NACA

RESEARCH MEMORANDUM

AERODYNAMICS OF SLENDER BODIES AT MACH NUMBER OF 3.12 AND REYNOLDS NUMBERS FROM 2×10^6 TO 15×10^6

I - BODY OF REVOLUTION WITH NEAR-PARABOLIC FOREBODY AND CYLINDRICAL AFTERBODY

By John R. Jack and Warren C. Burgess

Lewis Flight Propulsion Laboratory
Cleveland, Ohio

NATIONAL ADVISORY COMMITTEE
FOR AERONAUTICS

WASHINGTON
November 13, 1951

NATIONAL ADVISORY COMMITTEE FOR AERONAUTICS

RESEARCH MEMORANDUM

AERODYNAMICS OF SLENDER BODIES AT MACH NUMBER OF 3.12 AND REYNOLDS NUMBERS FROM 2×10^6 TO 15×10^6

I - BODY OF REVOLUTION WITH NEAR-PARABOLIC FOREBODY AND CYLINDRICAL AFTERBODY

By John R. Jack and Warren C. Burgess

SUMMARY

An experimental investigation to determine the aerodynamic characteristics of a slender, square-based body of revolution was conducted in the NACA Lewis 1- by 1-foot supersonic wind tunnel. Pressure distributions, viscous drag, and three component forces were measured at a Mach number of 3.12 for a Reynolds number range of 2×10^6 to 15×10^6 and for an angle-of-attack range of 0° to 10°.

The pressure distribution over the nose of the body for the small angles of attack and for Reynolds numbers greater than 8×10^6 agreed well with those predicted by linearized theory. For the large angles of attack, the agreement was poor, especially for the top surface of the model where the effects of cross-flow separation became important. The base-pressure coefficient for zero angle of attack decreased uniformly with increasing Reynolds number until a Reynolds number of 6×10^6 was reached, after which the base-pressure coefficient remained relatively constant.

The force measurements of the investigation showed that the drag coefficient for zero angle of attack increased with increasing Reynolds number until a Reynolds number of 6.5×10^6 was reached. Further increases in Reynolds number had little effect on the drag coefficient. The lift and pitching-moment coefficients increased uniformly with increasing angle of attack and were essentially independent of Reynolds number. A separation of the measured total-drag coefficient into components at zero angle of attack showed that the fore-pressure-drag coefficient was approximately one-sixth, the base-pressure-drag coefficient was approximately one-half, and the skin-friction-drag coefficient was approximately one-third of the total drag.

Trends similar to those of the experimental data were predicted by Allen's method, which includes some effects of viscosity; however, this

method underestimated the increment in fore-drag coefficient due to angle of attack, the lift coefficient, and the pitching-moment coefficient. Potential theory was inferior to Allen's method for predicting the force coefficients.

INTRODUCTION

Existing experimental data for low supersonic Mach numbers (for example, references 1 to 3) indicate that the linearized potential theory adequately predicts the pressure distribution for zero angle of attack, but that it fails to predict accurately the incremental pressure distributions and over-all forces resulting from inclined flow. A more complete equation is obtained in reference 1 for the incremental pressure distributions resulting from moderate angles of attack, but the agreement with experimental force measurements is still poor. The semiempirical theory of reference 4, which employs the concept of the viscous cross flow, has proved somewhat more successful in predicting the body forces encountered at low supersonic Mach numbers. The present investigation was undertaken at the NACA Lewis laboratory to complement the basic aerodynamic data available at high Mach numbers by evaluating the effect of Reynolds number and angle of attack on the pressure distributions and forces on a slender, square-based body of revolution at a Mach number of 3.12.

Pressure distributions over the body and the forces acting on the body have been determined experimentally for a range of Reynolds numbers from 2×10^6 to 15×10^6 and angles of attack from 0° to 10°. These data are compared with linearized potential theory and the semiempirical method of reference 4. In order to provide a more complete correlation of experimental data and to evaluate the effects of viscosity, the boundary-layer growth was investigated along the length of the model.

SYMBOLS

The following symbols are used in this report:

A_b base area

A_F frontal area

A_P plan-form area

A_W wetted area

C_D drag coefficient, D/q_0A_F

ΔC_D increment of drag coefficient due to angle of attack

C_L	lift coefficient, $L/q_0 A_F$
C_M	pitching-moment coefficient about base of model, $M/q_0 A_F l$
C_p	pressure coefficient, $(p-p_0)/q_0$
$C_{p,\alpha}$	pressure coefficient increment due to angle of attack
D	drag
d	body diameter
F	fineness ratio
L	lift force
l	body length
M	pitching moment
P_0	free-stream total pressure
p	static pressure
q	dynamic pressure, $(\gamma/2)\, p_0 M_0^2$
Re	Reynolds number, $\rho_0 U_0 l/\mu$
Re_x	Reynolds number based on length x
U_0	free-stream velocity
u	velocity in boundary layer
V	volume of body
x,r,θ	cylindrical coordinates
α	angle of attack
γ	ratio of specific heats, 1.40
δ^*	displacement thickness, $\frac{1}{\rho_1 u_1}\int_0^\infty (\rho_1 u_1 - \rho u)\, dy$
θ	momentum thickness, $\frac{1}{\rho_1 u_1^2}\int_0^\infty \rho u(u_1 - u)\, dy$

μ	viscosity
ρ	density
ϕ	velocity potential

Subscripts:

0	free-stream conditions
1	conditions at edge of boundary layer
B	body
b	base
f	friction
M	measured value
m	maximum
n	nose
p	pressure

APPARATUS AND PROCEDURE

The investigation was conducted in the NACA Lewis 1- by 1-foot variable Reynolds number tunnel, which is a nonreturn-type tunnel with a test-section Mach number of 3.12 ± 0.03. A stagnation temperature of approximately 55° F was maintained throughout the investigation, and inlet pressures were varied from 6 to 52 pounds per square inch absolute. The entering air had a specific humidity of approximately 2×10^{-5} pounds of water per pound of dry air, insuring negligible condensation effects.

A schematic diagram of the model (fineness ratio, 12) is presented in figure 1. The first half of the model is defined by the equation

$$\frac{d}{d_m} = \left[2\left(\frac{2x}{l}\right) - \left(\frac{2x}{l}\right)^2\right]^{3/4} \tag{1}$$

This equation describes a closed body, which, according to reference 5, has a minimum wave drag for a given volume and length. The last half of the body is a cylindrical section. Pertinent geometric parameters of this model are given in the following table:

Body length, l, ft	1.75
Body fineness ratio, F_B	12
Nose fineness ratio, F_n	6
Volume of body, V, cu ft	0.0232
Wetted area, A_W, sq ft	0.688
Frontal area, A_F, sq ft	0.0167
Base area, A_b, sq ft	0.0167
Plan-form area, A_p, sq ft	0.219
Maximum body diameter, d_m, ft	0.146

The body used for pressure-distribution measurements and boundary-layer surveys was turned from mild steel and polished to a 5- to 8-microinch finish. The static-pressure orifices on the model surface were arranged in five rows and were located at stations given in figure 1. The boundary-layer data for zero angle of attack were obtained with the probe pictured in figure 2(a) and the data for the pitot contours were obtained from a traverse with the rake pictured in figure 2(b). Because intense sporadic vibrations of the model occurred at a Reynolds number of 15×10^6 and an angle of attack of 10°, pressure measurements were not made at this condition. Static pressures were measured on differential manometers to within ±0.002 pound per square inch absolute.

The force model was the same as the pressure distribution model except that it was turned from aluminum and had a 20-microinch finish. The model was rigidly connected to a three-component strain-gage balance, which was attached to a sting-strut combination. Since the strain gage was mounted internally, no aerodynamic tare corrections were necessary. Static calibration of the balance indicated that there was a slight interaction between the axial force and the moment; therefore, corrections for this interaction were made in the reduction of the force data. Forces were measured to within ±0.1 pound for drag, ±0.1 pound for lift, and ±0.5 inch-pound for pitching moment.

The models were supported from their bases by a sting extending upstream from a horizontal strut mounted to the side wall of the tunnel (fig. 3). The sting was designed by using the data presented in reference 6 for obtaining minimum interference with the base pressures at zero angle of attack. Angle of attack was varied by rotating the model about a point 4 inches upstream of the base.

REDUCTION OF DATA AND METHODS OF COMPUTATION

In the reduction of the pressure data, the free-stream static pressure was assumed to be the static pressure measured on the tunnel wall opposite the model tip. Correction for the axial gradient of free-stream static pressure measured on the tunnel side walls was negligible, and hence was not applied to the results.

The incremental pressure coefficient due to angle of attack $C_{p,\alpha}$ was obtained by subtracting the measured values at zero angle of attack from the measured values at angle of attack.

The boundary-layer-survey data were evaluated by the Rankine-Hugoniot equation with the assumption that the total temperature was constant in the flow field, and that the static pressure was constant along radial lines through the boundary layer.

Skin-friction coefficients were calculated using the following equation:

$$C_{D,f} = \frac{2\pi}{q_0 A_F}\left[\int_0^s \frac{d(r\rho_1 u_1^2\theta)}{ds}\,ds - \int_0^s r\delta^*\frac{dp}{ds}\,ds\right] \tag{2}$$

where

$$\theta = \frac{1}{\rho_1 u_1^2}\int_0^\infty \rho u(u_1-u)\,dy \tag{3}$$

and

$$\delta^* = \frac{1}{\rho_1 u_1}\int_0^\infty (\rho_1 u_1 - \rho u)\,dy \tag{4}$$

and where s represents the distance measured along the surface of the body and y, the distance measured normal to the body surface. This equation may be derived from the boundary-layer momentum equation for axially symmetric bodies under the assumption that δ is very much less than the body radius.

The theoretical pressure-distribution curves were calculated by the numerical method of reference 7. The following equations were used to calculate the pressure coefficients:

$$C_p = -\frac{2}{U_0}\frac{\partial \phi}{\partial x} - \left(\frac{dr}{dx}\right)^2 \tag{5}$$

$$C_{p,\alpha} = 4\alpha\cos\theta\frac{dr}{dx} + \alpha^2(1-4\sin^2\theta) \tag{6}$$

The theoretical force coefficients were calculated by the method of reference 4, wherein viscous effects are estimated. The equations given in reference 4 for the force and moment coefficients are:

$$\Delta C_D = \alpha^2 + \eta C_{d,c} \frac{A_P}{A_F} \alpha^3 \tag{7}$$

$$C_L = 2\alpha + \eta C_{d,c} \frac{A_P}{A_F} \alpha^2 \tag{8}$$

$$C_M = 2 \frac{V}{A_F l} \alpha + \eta C_{d,c} \frac{A_P}{A_F} \left(\frac{l - x_P}{l}\right) \alpha^2 \tag{9}$$

where x_P is the centroid of the plan area, η is the ratio of the drag coefficient of a circular cylinder of finite length to that of a cylinder of infinite length, and $C_{d,c}$ is the section drag coefficient of a circular cylinder per unit length. From reference 4 a value for η of 0.70 and a representative value for $C_{d,c}$ of 1.20 were obtained for the cross-flow Reynolds numbers encountered in this investigation.

RESULTS AND DISCUSSION

The experimental results consist of pressure distributions on the forebody and base surface, boundary-layer surveys for several axial stations, and force measurements. These results are discussed in order for zero angle of attack and for angle of attack.

Forebody Pressure Distributions

Zero angle of attack. - The experimental variation of the pressure coefficient with axial position on the body for three Reynolds numbers is presented in figure 4. Theoretical curves computed from the linearized theory of reference 7 are compared with the experimental data.

The trends for the experimental and theoretical curves were similar for all Reynolds numbers. For the lower Reynolds numbers the agreement between theory and experiment was good only for the first 40 percent of the nose. As the Reynolds number was increased from 2×10^6 to 8×10^6 (figs. 4(a) and 4(b)), the agreement between experiment and theory improved, particularly on the cylindrical portion of the model; however, with a further increase in Reynolds number to 15×10^6, very little improvement was noticed. Evaluating the theoretical pressure distribution in terms of the body diameter plus the measured boundary-layer

displacement thickness resulted in a negligible change in the theoretical distribution. The improvement in agreement between experiment and theory upon increasing the Reynolds number from 2×10^6 to 8×10^6, however, corresponded to a movement of the beginning of transition from the base of the model to a point 15 inches upstream of the model base. The data for the side pressure distributions show evidence of a disturbance existing in the tunnel free-stream flow; consequently, the preceding conclusions were based on the bottom profile. This disturbance as well as that to be mentioned subsequently for angle of attack is attributed to irregularities in the tunnel flow. Because corrections of these nonuniformities would require considerably more calibration data than are now available, no attempt was made to evaluate the effect herein. The disturbance affecting the side-pressure distribution at zero angle of attack was evaluated in terms of over-all drag and at most gave an error of approximately 1 percent.

Angle of attack. - The axial pressure distributions along the top and bottom of the model are presented in figure 5 for three angles of attack and three Reynolds numbers. The pressure-coefficient increments due to angle of attack, as determined from figures 4 and 5, are compared in figure 6 with the slender-body theory of reference 1.

On the bottom surface of the model (figs. 6(a), 6(b), and 6(c)), experiment and theory have similar trends, but the agreement becomes progressively worse as the angle of attack increases. (The humps in the curves are attributed to the tunnel disturbance mentioned previously.) The effect of Reynolds number upon the agreement was negligible at 3° angle of attack. At the higher angles of attack, no definite Reynolds number effect was observable.

On the top surface of the model (figs. 6(d), 6(e), and 6(f)), the effect of increasing the angle of attack was to decrease the pressures on the nose section in a manner similar to that predicted by theory. The theoretical curves for $\alpha = 3^\circ$, 8°, and 10° cross each other, whereas the experimental curves do not. The difference between experiment and theory for the cylindrical portion of the model increased as the angle of attack increased. This result is attributed to cross-flow separation which will be discussed later.

Some improvement in the agreement between experiment and theory with increasing Reynolds number was observed on the forward part of the nose; however, the change in the agreement for the rest of the body was negligible.

Experimental pressure distributions as a function of the meridian angle around the body are given in figure 7 for three axial stations and three Reynolds numbers. Since no conclusive Reynolds number effect was obtained, only the experimental pressure increments due to angle

of attack for a Reynolds number of 15×10^6 are compared with theory in figure 8. Agreement between experiment and theory is good for $\alpha = 3^\circ$ but poor for $\alpha = 8^\circ$.

Base Pressures

The variation of base-pressure coefficient with Reynolds number is presented in figure 9. In figure 9(a) the measured coefficients at zero angle of attack are compared with the coefficients predicted by the method of reference 8. The method of reference 8 predicts the correct trend, but underestimates the measured values by more than 10 percent. However, in terms of over-all drag this discrepancy amounts to only 5 percent.

The variation of base-pressure coefficient with free-stream Reynolds number for 0°, 3°, 6°, 8°, and 10° angles of attack is presented in figure 9(b). For zero angle of attack, the base-pressure coefficient decreases with increasing Reynolds number until a Reynolds number of 6×10^6 is reached and then remains relatively constant. With increasing angle of attack, the Reynolds number at which the pressure becomes constant increases to approximately 12×10^6 for $\alpha = 8^\circ$.

Figure 10 shows the variation of the base-pressure coefficient with angle of attack for five Reynolds numbers. The base-pressure coefficients for the highest Reynolds numbers decrease as the angle of attack increases; however, for the two low Reynolds numbers, the pressure coefficient first increases to a maximum near $\alpha = \pm3^\circ$ and then decreases for higher angles of attack. The broken line between the $\alpha = \pm3^\circ$ data is used to indicate that the true variation of the pressure coefficient in this region is unknown. This behavior for the low Reynolds numbers may be associated with the movement of the boundary-layer-transition region with increasing angle of attack which will be discussed more fully later. The cross-over of the curves presented in figure 9(b) may also be attributed to the movement of the boundary-layer-transition region with angle of attack.

Boundary Layer and Cross-Flow Separation

Skin friction. - In order to complete the investigation of the component drag forces which make up the total drag of the body at $\alpha = 0^\circ$, friction-drag coefficients were obtained from the experimentally determined displacement and momentum thicknesses for Reynolds numbers of 4×10^6, 8×10^6, and 14×10^6. The experimental mean friction-drag coefficients $C_{D,f}$ for different axial stations are presented in figure 11 for the preceding free-stream Reynolds numbers.

A comparison of the measured $C_{D,f}$ with the corresponding compressible-flat-plate coefficients is also given in figure 11. The laminar coefficient (reference 9) and the turbulent mean friction-drag coefficients (reference 10) are presented as follows:

$$\text{laminar} \quad C_{D,f} = \frac{1.207}{Re^{1/2}} \tag{10}$$

$$\text{turbulent} \quad C_{D,f} = \frac{0.0306}{\left(1 + \frac{M_0^2}{10}\right)^{5/7} Re^{1/7}} \quad \text{(based on arithmetic mean temperature)} \tag{11}$$

$$\text{turbulent} \quad C_{D,f} = \frac{0.0306}{\left(1 + \frac{M_0^2}{5}\right)^{5/7} Re^{1/7}} \quad \text{(based on wall temperature)} \tag{12}$$

The theoretical laminar skin friction for a cone as derived in reference 11 is

$$C_{D,f} = \frac{2}{\sqrt{3}} \frac{1.207}{Re^{1/2}} \tag{13}$$

This equation is also presented in figure 11 for comparison.

A quantitative comparison between the flat-plate coefficients and the measured coefficients on a body of revolution is subject to question. However, if the effect of pressure gradient on skin-friction drag is of secondary importance (reference 9), a comparison of the measured values with the conical values is reasonable. The good agreement between the experimental and theoretical coefficients of Mangler (reference 11) indicates that the effect of the pressure gradient along the body was small (fig. 11). The experimental coefficients for values of Re_x beyond transition tend to approach the empirical coefficients for fully turbulent boundary layers based on wall temperature (equation (12)) rather than those based on arithmetic mean temperature (equation (11)). This, however, does not indicate that equation (12) is more applicable than equation (11), inasmuch as the empirical formulas have not been corrected for the effect of the initial laminar boundary layer or for the difference between axially symmetric and flat-plate flow.

The momentum- and displacement-thickness distributions which were used in obtaining the experimental friction coefficients of figure 11 are presented in figure 12.

Boundary-layer transition. - In the course of the investigation of the effect of Reynolds number upon friction drag, boundary-layer transition was investigated at zero angle of attack. The beginning of the boundary-layer-transition region was determined from microsecond schlieren photographs as indicated in figure 13. The variation of the axial distance to the beginning of transition (equivalent to the extent of laminar boundary layer) with Reynolds number for zero angle of attack is presented in figure 14(a).

The schlieren transition data were substantiated with a probe investigation of the boundary layer by measuring the momentum and displacement thicknesses at one station over a range of Reynolds numbers (fig. 15). The critical Reynolds number was chosen to be the value at which the friction drag coefficient and consequently the momentum thickness started to increase. The critical Reynolds number of figure 15 is presented in figure 14 (square symbol) for a comparison of the two techniques. As anticipated, the axial extent of the laminar boundary layer decreased with increasing Reynolds number (fig. 14(a)). The critical Reynolds number, defined as free-stream Reynolds number per foot times the axial distance to the beginning of transition, increased with increasing inlet pressure, as shown in figure 14(b). It is known that reservoir conditions influence the critical Reynolds number in incompressible flow, and hence it is suggested that the trend of figure 14(b) may be caused by a change in the turbulence level or tunnel boundary-layer development with a change in inlet air pressure.

The effect of angle of attack upon boundary-layer transition is presented in figure 16 for a Reynolds number of 8×10^6. It is evident from the figure that transition is retarded on the bottom region of the model and accelerated on the upper region at positive angles of attack. This effect may be attributed to the fact that the low-energy air of the boundary layer moves from the bottom surface of the model towards the top surface.

Cross-flow separation. - Cross-flow separation was observed from schlieren data and investigated by pitot surveys. This phenomenon has been observed with pitot surveys at the model base (reference 1) and with a "vapor screen" method (reference 12). Pitot surveys at three axial stations on the cylindrical portion of the body and the corresponding schlieren photograph of the flow field are presented in figure 17 for the body at an angle of attack of 8° ($Re = 8\times10^6$). Although the values of P_M/p_0 in figure 17 are of little quantitative significance, they serve to locate the vortices associated with cross-flow separation, and consequently, the regions of low-energy air. The bulge in the 0.25 P_M/P_0 curve near the side of the body at stations A and B may be attributed to the downstream portion of the disturbance in the tunnel flow field previously mentioned in connection with the forebody pressure distributions.

Schlieren observations of cross-flow separation at 8° angle of attack are presented in figure 18 for Reynolds numbers of 4×10^6, 8×10^6, 12×10^6, and 15×10^6. The figure shows that no large Reynolds number effect exists.

Force Measurements

Zero angle of attack. - The experimental variation of total drag with Reynolds number obtained with the force model is given in figure 19. The contributions to total drag of fore-pressure, base-pressure, and skin-friction drags as measured on the pressure-distribution model are also presented. The total-drag coefficient increased with increasing Reynolds number until a Reynolds number of 6.5×10^6 was reached and then leveled off at a value of approximately 0.21. As shown in figure 19 the fore-pressure drag is approximately one-sixth, the base-pressure drag is approximately one-half, and the skin-friction drag is approximately one-third of the total drag. The maximum difference between the summation of the components and the total-drag coefficient measured with the strain-gage balance is 13.6 percent. Schlieren photographs indicated that transition occurred farther upstream for the force model than for the pressure-distribution model; the force model, consequently, had a greater skin-friction-drag coefficient and thus a greater total-drag coefficient than the pressure-distribution model. If the pressure drags of the force and pressure models are assumed to be the same, the variation of skin-friction-drag coefficients with Reynolds number for both models is presented in figure 20. Figure 20 indicates that the difference between the total forces can be accounted for by the forward movement of transition. This discrepancy, in part, may be attributed to the difference in model surface finishes.

Angle of attack. - The total-drag coefficient and the increment in fore drag due to angle of attack are plotted in figure 21 as functions of angle of attack for various Reynolds numbers. The dependence of drag on Reynolds number is also indicated. At an angle of attack of 10°, the value of C_D for a Reynolds number of 15×10^6 is 4.5 percent lower than the value for a Reynolds number of 2×10^6. The theoretical curve obtained by the method of reference 4 is compared with the increment in drag due to angle of attack. The data show that the method of reference 4 greatly underestimates the experimental values.

The lift coefficient (fig. 22) is much greater at all Reynolds numbers than would be predicted by linearized potential theory. The method of reference 4 yields results closer to experimental values, but still underestimates the experimental values by a large percentage at all angles of attack. Figure 22 shows also that the variation of the lift coefficient with Reynolds number is very small.

The experimental and theoretical lift distributions over the body are given in figure 23 for two angles of attack. The large difference between the potential lift distributions and the experimental lift distributions is attributed, in part, to the inherent inadequacy of the potential theory to account for viscosity and, in part, to the use of the first-order potential flow theory. The experimental curves which were obtained from the pressure distribution data at $Re = 8 \times 10^6$ have been integrated and the total lift coefficient has been plotted on figure 22. As shown in figure 22, the integrated values fall somewhat below the values measured by the strain-gage balance. This difference may be attributed to the fact that the cross-flow skin-friction drag, which has a component acting in the lift direction, has not been added to the integrated pressure value, or it may be attributed to insufficient instrumentation of the model.

The experimental and theoretical variation of the pitching-moment coefficient about the base of the model with angle of attack is given in figure 24. The effect of Reynolds number, as in the case of the lift coefficient, is small.

A comparison of the experimental values with those predicted by the method of reference 4 shows that for an angle of attack of 10° the coefficient of pitching moment is underestimated by 20 percent. Since the slope of the lift curve increased with angle of attack at a faster rate than the slope of the pitching-moment curve, the center of pressure moved rearward as shown in figure 25. The center of pressure, as predicted by the method of reference 4, is upstream of the measured center of pressure by 1/2 diameter at an angle of attack of 3° and 1 diameter at an angle of attack of 10°.

SUMMARY OF RESULTS

The aerodynamic characteristics of a slender, square-based body of revolution were investigated in the NACA Lewis 1- by 1-foot variable Reynolds number tunnel at a Mach number of 3.12. The results may be summarized as follows:

Pressure Distributions

1. The pressure distributions on the nose of the model for zero angle of attack and for Reynolds numbers greater than 8×10^6 agreed closely with those predicted by linearized potential theory. For lower Reynolds numbers, the agreement was good only for the first 40 percent of the nose.

2. The experimental pressure distributions due to angle of attack on the top and bottom surfaces of the model agreed well with theory for small angles of attack. For large angles of attack, the agreement was poor, especially for the top surface of the model, indicating that cross-flow separation becomes important in this region.

3. For zero angle of attack, the base-pressure coefficient decreased with increasing free-stream Reynolds number until a free-stream Reynolds number of 6×10^6 was reached and then remained relatively constant. The base pressures for angle of attack followed the same trend.

4. A method derived by Cope of the National Physical Laboratory predicted the correct trend for base-pressure coefficient at zero angle of attack but underestimated the measured values by more than 10 percent.

5. At low Reynolds numbers the base-pressure coefficient first increased and then decreased as the angle of attack was increased. The maximum pressure was obtained at an angle of attack of about 3°. For high Reynolds numbers the base-pressure coefficient decreased uniformly with increasing angle of attack.

Boundary Layer

1. The measured mean skin-friction coefficients for laminar flow over the nose of the model agreed well with the theoretical values predicted by Mangler for laminar flow over cones.

2. No Reynolds number effect upon cross-flow separation was visible for Reynolds numbers from 4×10^6 to 15×10^6.

Forces

1. The drag coefficient for zero angle of attack increased with increasing Reynolds number until a Reynolds number of 6.5×10^6 was reached and then remained relatively constant.

2. The lift and pitching-moment coefficients increased uniformly as the angle of attack was increased and were relatively independent of Reynolds number.

3. A breakdown of the measured total drag into components at zero angle of attack shows that the fore-pressure drag was approximately one-sixth, the base-pressure drag was approximately one-half, and the skin-friction drag was approximately one-third of the total drag at all Reynolds numbers.

4. Potential theory was inferior to Allen's method, which predicted trends similar to those of the experimental data but underestimated the increment in fore-drag coefficient due to angle of attack, the lift coefficient, and the pitching-moment coefficient.

Lewis Flight Propulsion Laboratory
National Advisory Committee for Aeronautics
Cleveland, Ohio

2269

REFERENCES

1. Luidens, Roger W., and Simon, Paul C.: Aerodynamic Characteristics of NACA RM-10 Missile in 8- by 6-Foot Supersonic Wind Tunnel at Mach Numbers from 1.49 to 1.98. I - Presentation and Analysis of Pressure Measurements (Stabilizing Fins Removed). NACA RM E50D10, 1950.

2. Esenwein, Fred T., Obery, Leonard J., and Schueller, Carl F.: Aerodynamic Characteristics of NACA RM-10 Missile in 8- by 6-Foot Supersonic Wind Tunnel at Mach Numbers from 1.49 to 1.98. II - Presentation and Analysis of Force Measurements. NACA RM E50D28, 1950.

3. Allen, H. Julian: Pressure Distribution and Some Effects of Viscosity on Slender Inclined Bodies of Revolution. NACA TN 2044, 1950.

4. Allen, H. Julian: Estimation of the Forces and Moments Acting on Inclined Bodies of Revolution of High Fineness Ratios. NACA RM A9I26, 1949.

5. Jones, Robert T.: Estimated Lift-Drag Ratios at Supersonic Speeds. NACA TN 1350, 1947.

6. Chapman, Dean R.: An Analysis of Base Pressure at Supersonic Velocities and Comparison with Experiment. NACA TN 2137, 1950.

7. von Kármán, Theodor, and Moore, Norton B.: Resistance of Slender Bodies Moving with Supersonic Velocities, with Special Reference to Projectiles. Trans. A.S.M.E., vol. 54, no. 23, Dec. 15, 1932, pp. 303-310.

8. Cope, W. F.: The Effect of Reynolds Number on the Base Pressure of Projectiles. Eng. Div. Rep. 63/44, Nat. Physical Lab., Jan. 1945.

9. von Kármán, Th., and Tsien, H. S.: Boundary Layer in Compressible Fluids. Jour. Aero. Sci., vol. 5, no. 6, April 1938, pp. 227-232.

10. Tucker, Maurice: Approximate Turbulent Boundary-Layer Development in Plane Compressible Flow Along Thermally Insulated Surfaces with Application to Supersonic-Tunnel Contour Correction. NACA TN 2045, 1950.

11. Mangler, W.: Compressible Boundary Layers on Bodies of Revolution. VG 83, No. 47T, M.A.P. Volkenrode.

12. Allen, H. Julian, and Perkins, Edward W.: Characteristics of Flow over Inclined Bodies of Revolution. NACA RM A50L07, 1951.

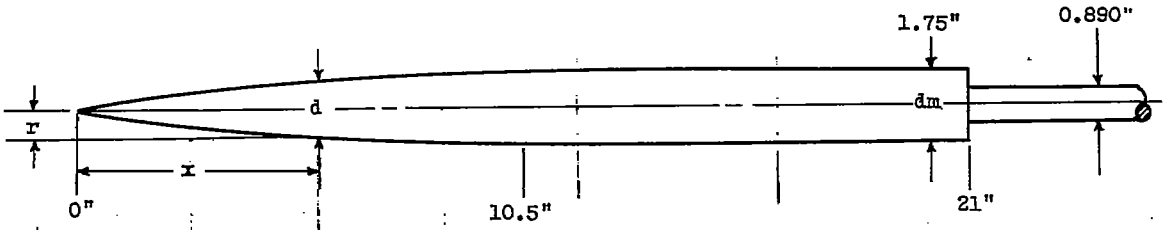

Model configuration

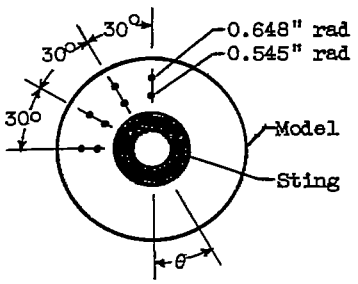

Base pressure orifices

Nose contour of body defined by:

$$\frac{d}{dm} = \left[2\left(\frac{2x}{l}\right) - \left(\frac{2x}{l}\right)^2\right]^{3/4}$$

where d_m is the maximum body diameter.

Location of surface static-pressure orifices

x (in.)	θ (deg)				
	0	22.5	45	67.5	90
1	x				x
2	x				x
3	x				x
4	x	x	x	x	x
5	x				x
6	x				x
7	x	x	x	x	x
8	x				x
9	x				x
9.5	x				x

x (in.)	θ (deg)				
	0	22.5	45	67.5	90
10	x				x
10.5	x	x	x	x	x
11	x				x
11.5	x				x
12	x				x
14	x	x	x	x	x
17	x				x
20	x				x
20.5	x	x	x	x	x

Figure 1. - Schematic drawing of model with location of static-pressure orifices.

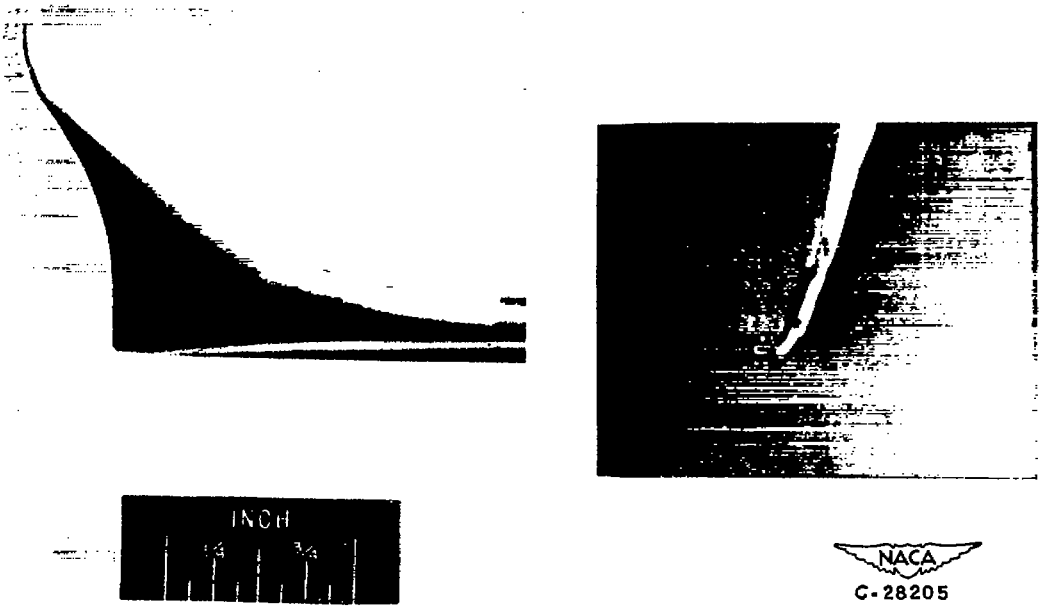

(a) Probe used to obtain boundary-layer data at zero angle of attack.

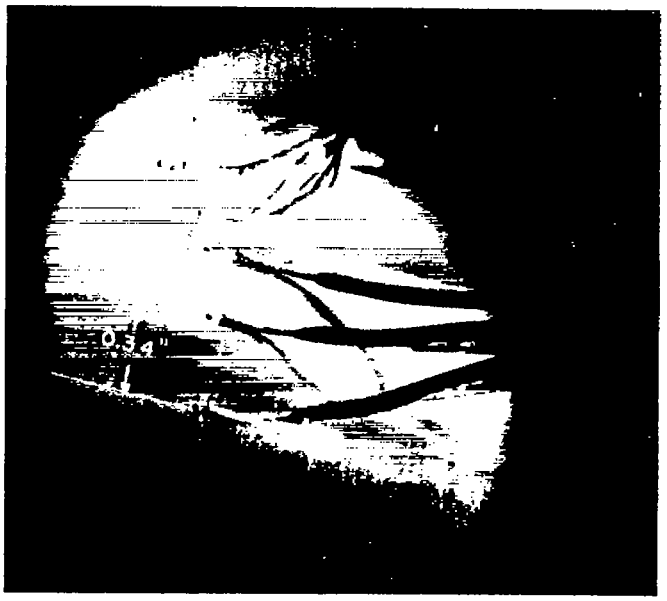

(b) Rake used for obtaining pitot pressure contours at angle of attack as viewed through port.

Figure 2. - Probe and rake used for surveys of boundary layer and cross-flow separation.

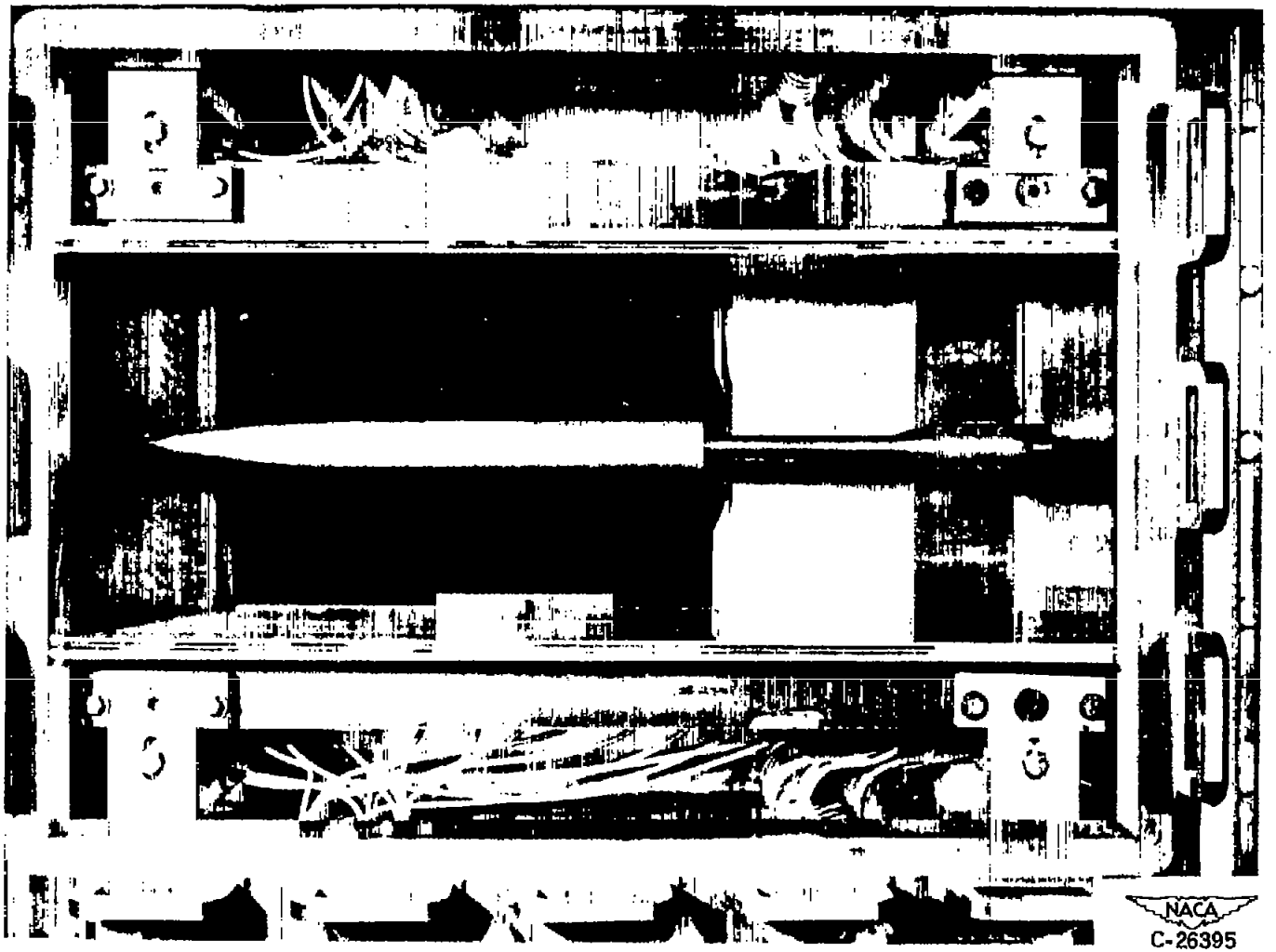

Figure 3. - Force model installed in Lewis 1- by 1-foot supersonic wind tunnel.

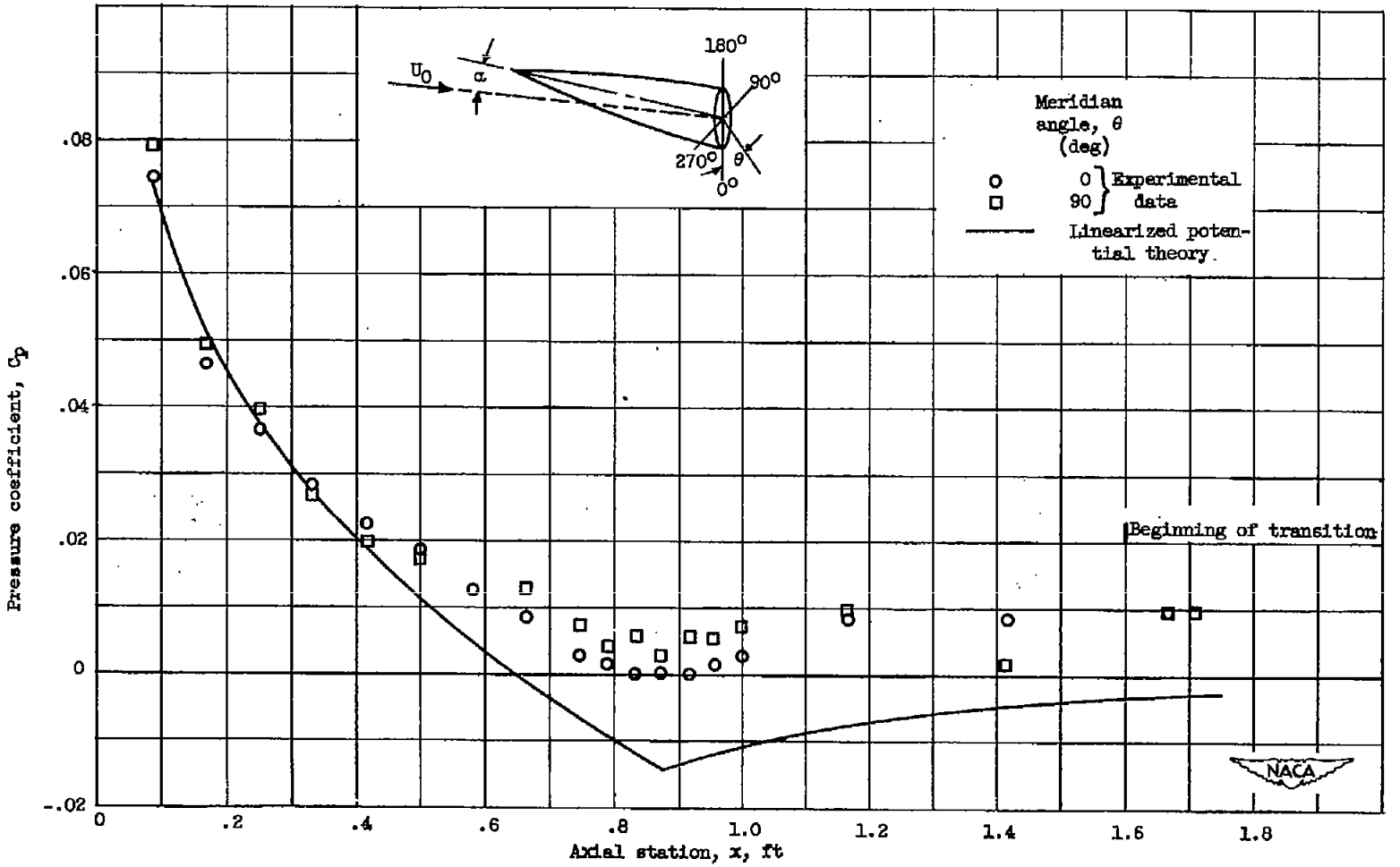

(a) Reynolds number Re, 2×10^6.

Figure 4. - Experimental and theoretical axial variation of pressure coefficient for model at zero angle of attack.

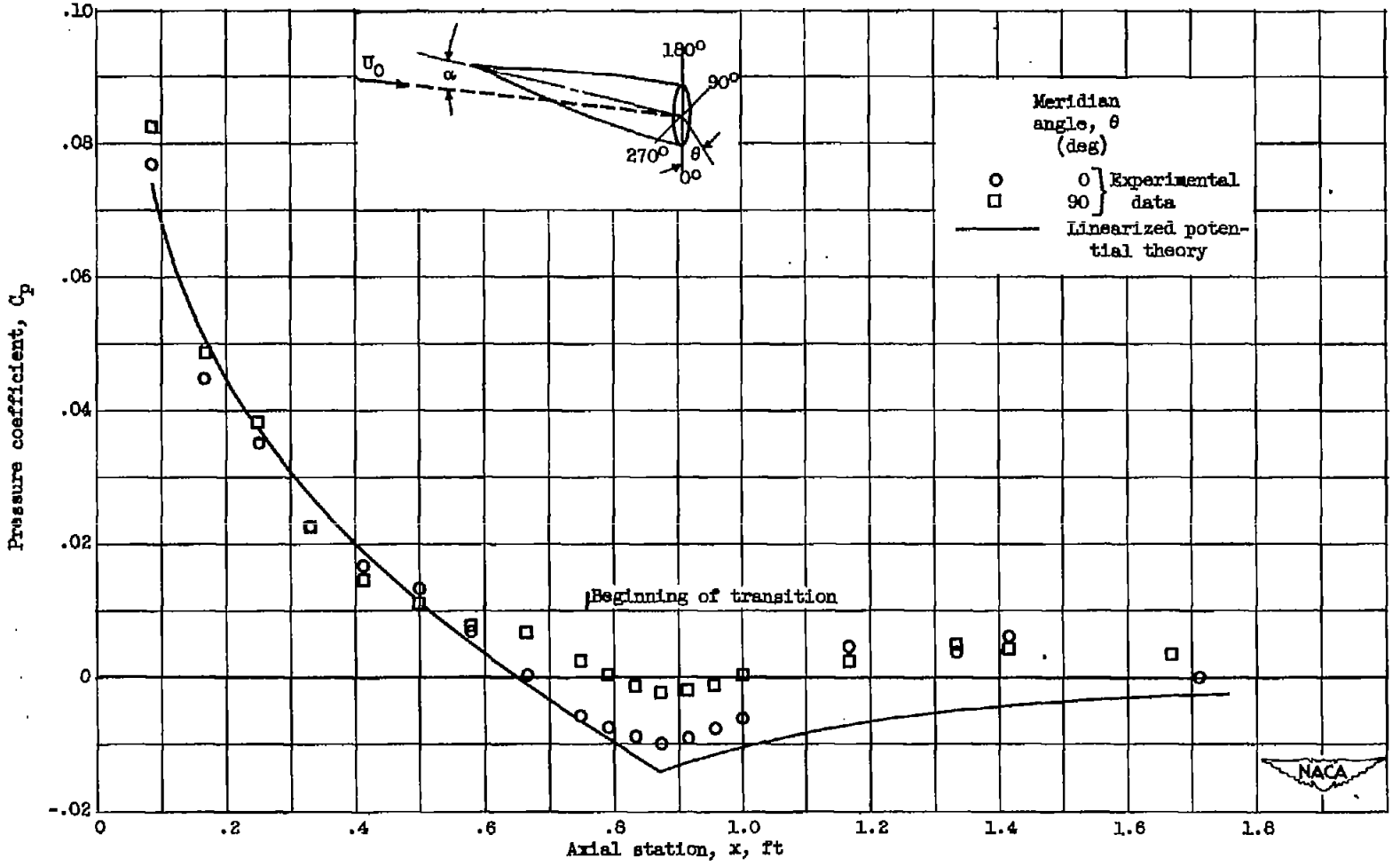

(b) Reynolds number Re, 8×10^6.

Figure 4. - Continued. Experimental and theoretical axial variation of pressure coefficient for model at zero angle of attack.

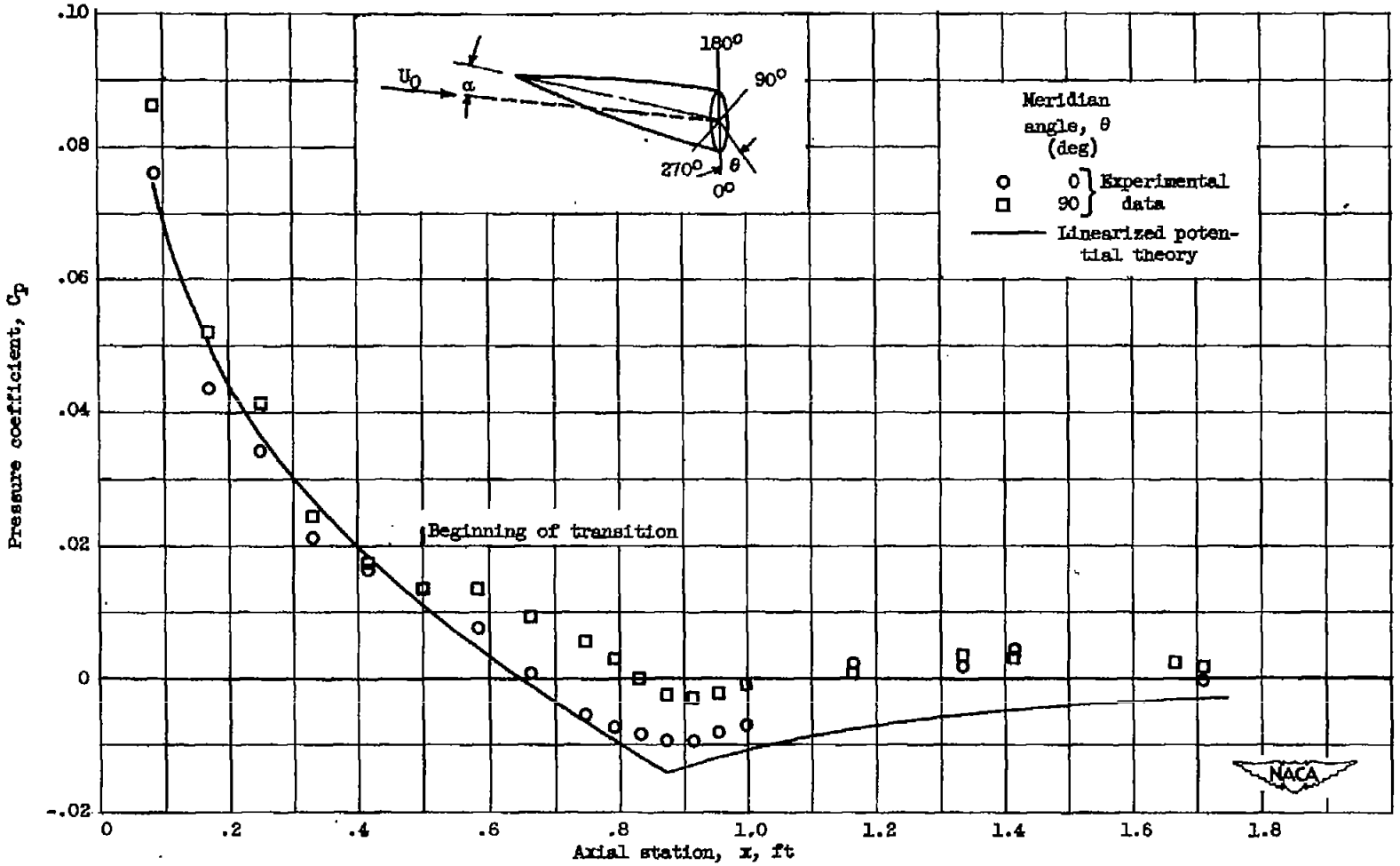

(c) Reynolds number Re, 15×10^6.

Figure 4. - Concluded. Experimental and theoretical axial variation of pressure coefficient for model at zero angle of attack.

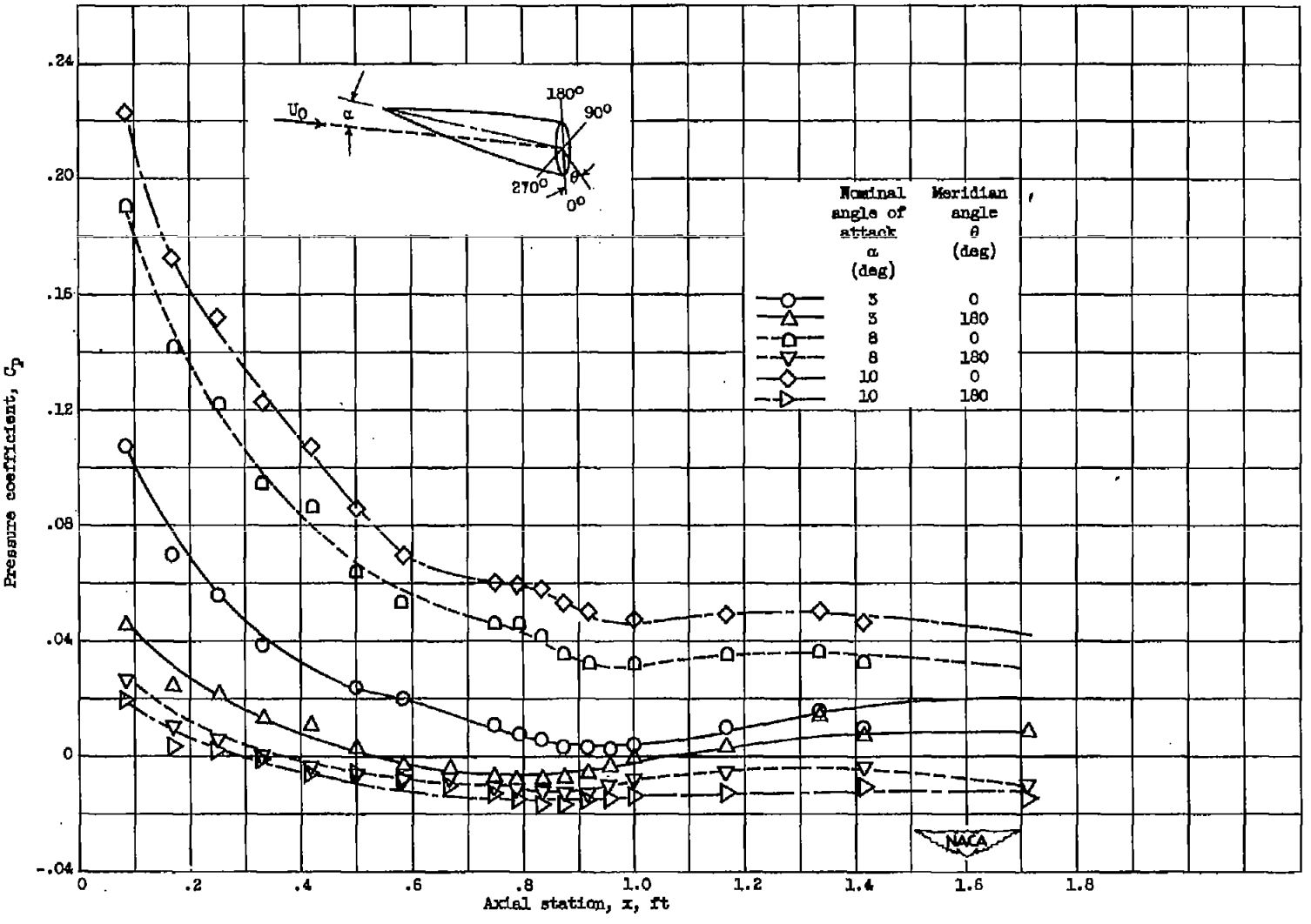

(a) Reynolds number Re, 2×10^6 for three angles of attack.

Figure 5. - Experimental axial variation of pressure coefficient.

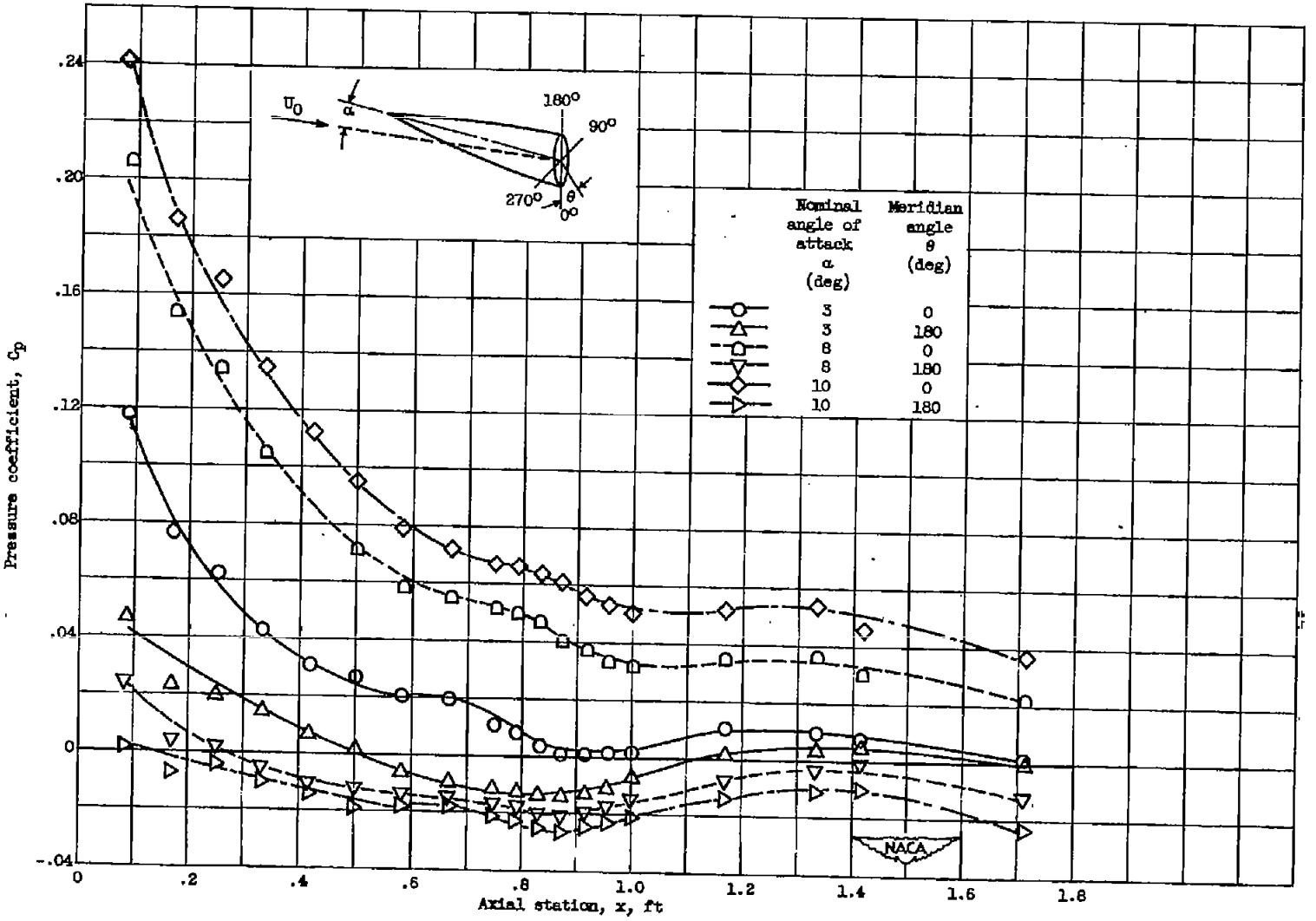

(b) Reynolds number Re, 8×10^6 for three angles of attack.

Figure 5. - Continued. Experimental axial variation of pressure coefficient.

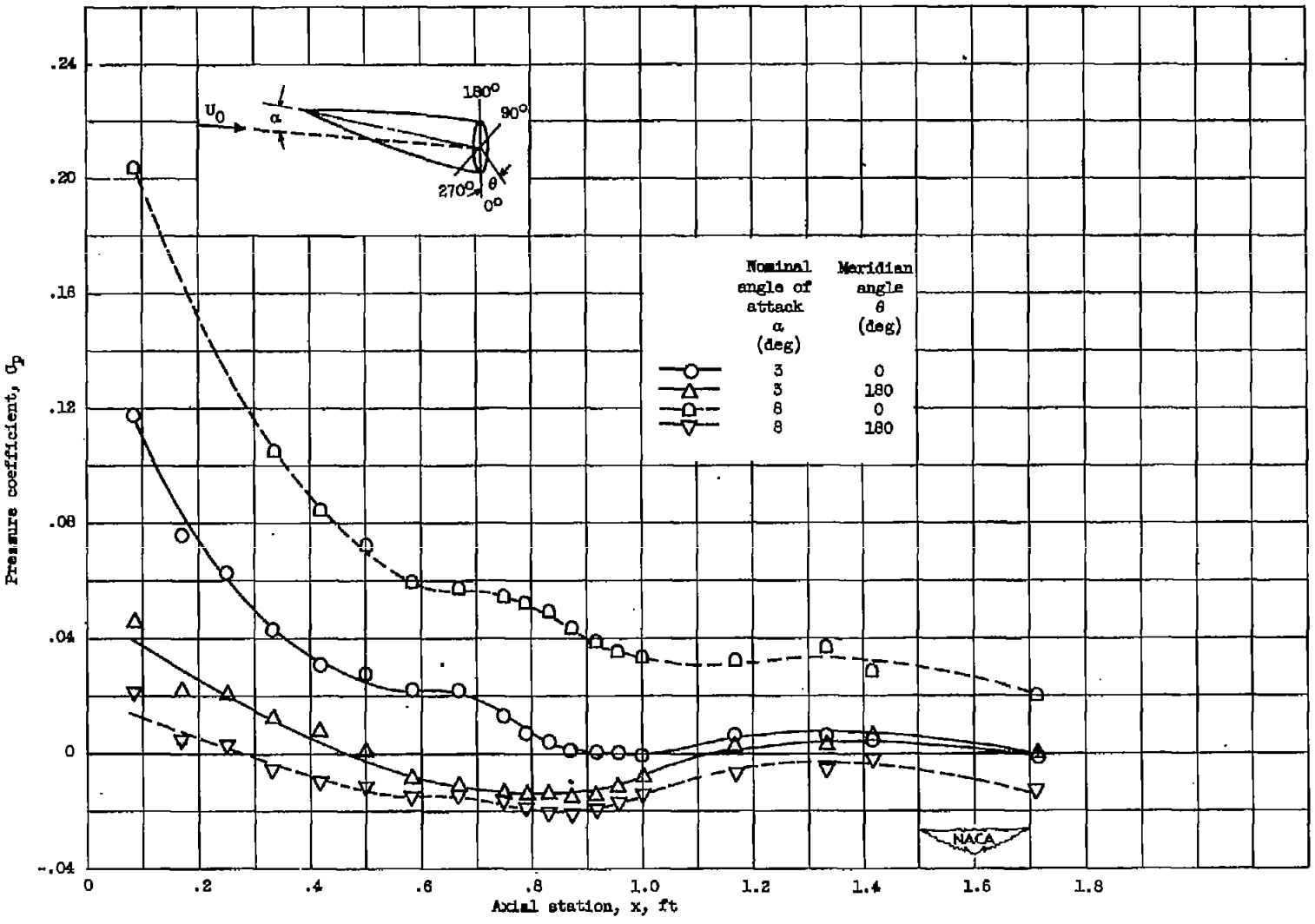

(c) Reynolds number Re, 15×10^6 for two angles of attack.

Figure 5. - Concluded. Experimental axial variation of pressure coefficient.

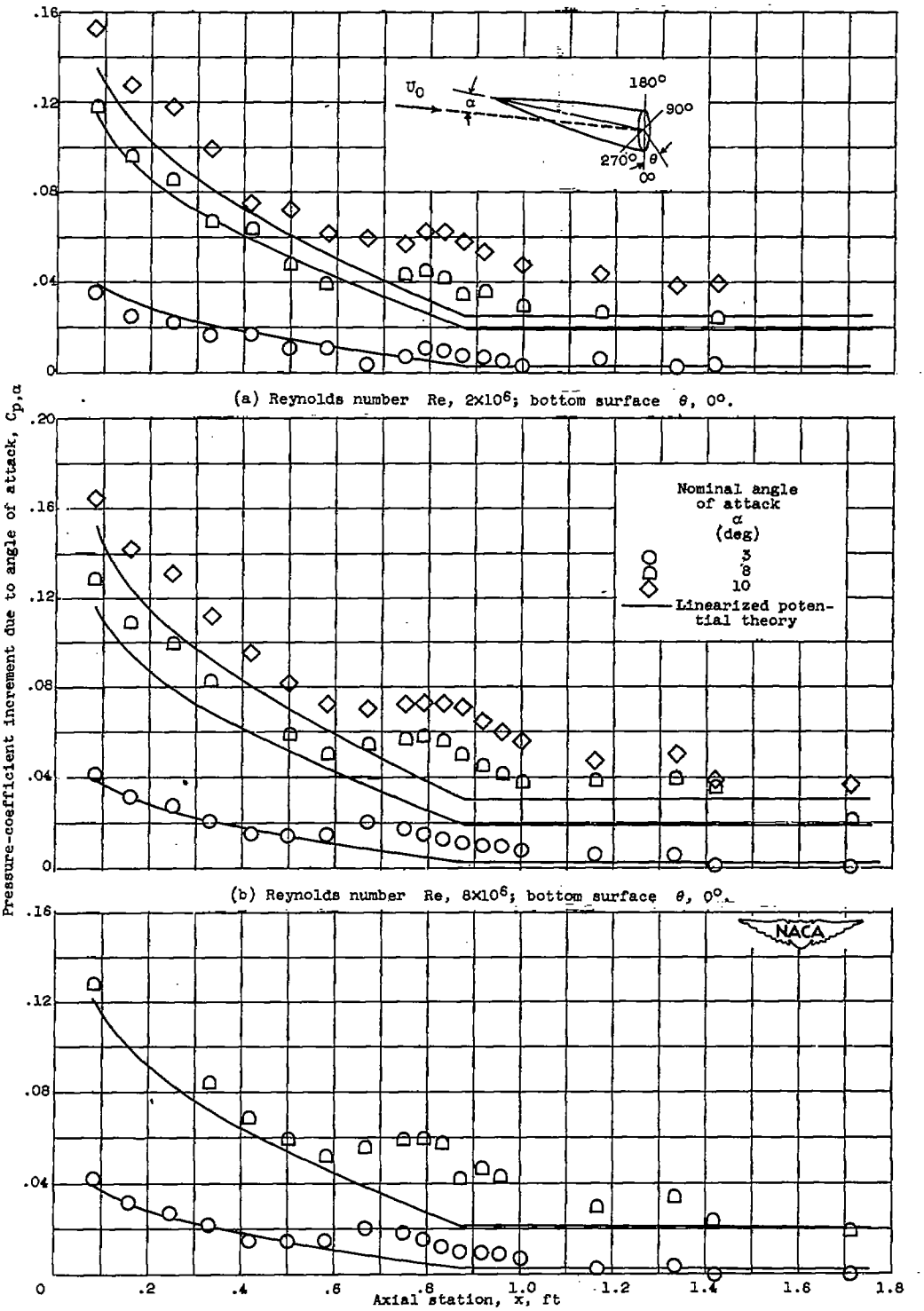

(a) Reynolds number Re, 2×10^6; bottom surface θ, 0°.

(b) Reynolds number Re, 8×10^6; bottom surface θ, 0°.

(c) Reynolds number Re, 15×10^6; bottom surface θ, 0°.

Figure 6. - Experimental and theoretical axial variation of pressure-coefficient increment due to angle of attack.

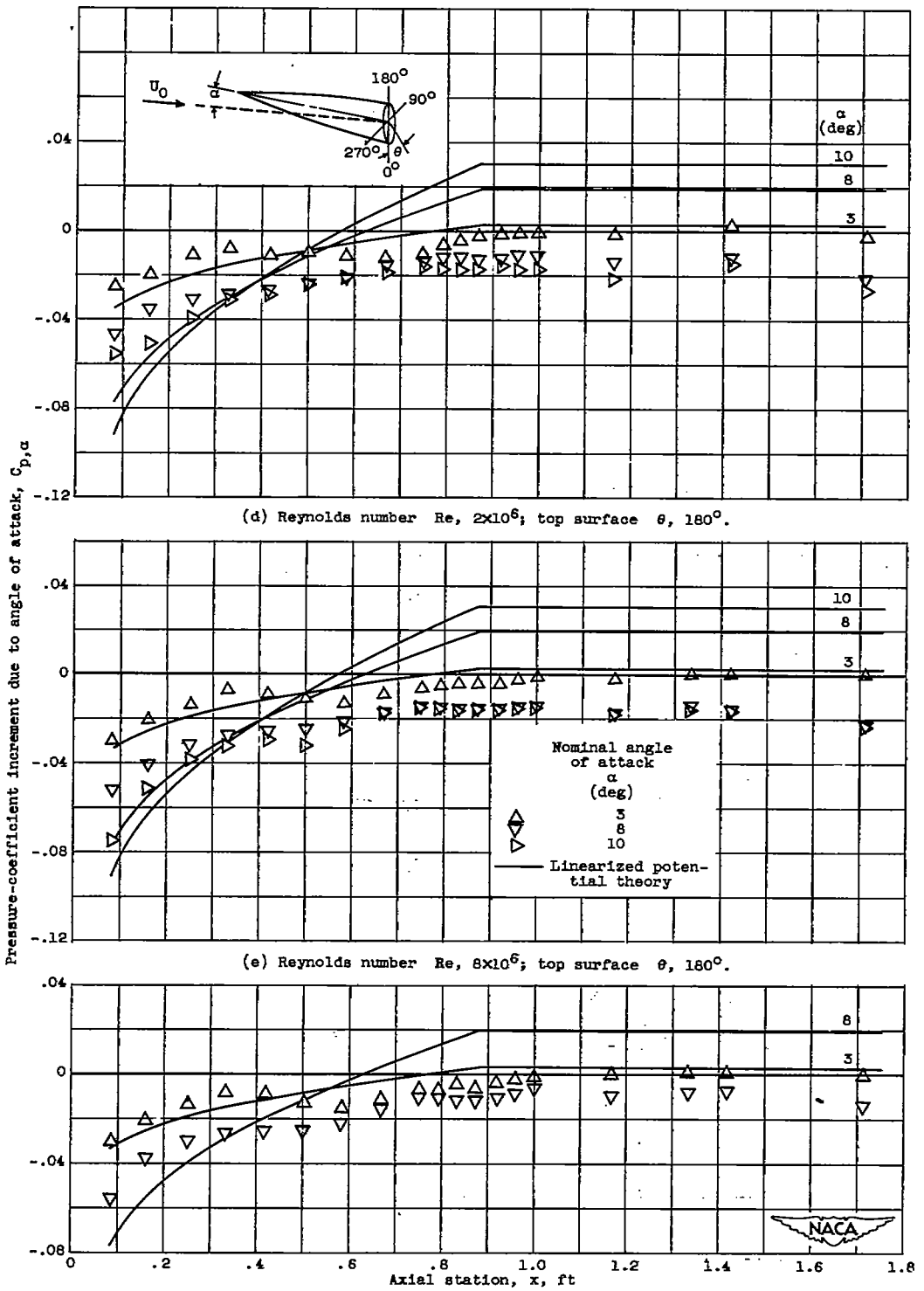

(d) Reynolds number Re, 2×10^6; top surface θ, 180°.

(e) Reynolds number Re, 8×10^6; top surface θ, 180°.

(f) Reynolds number Re, 15×10^6; top surface θ, 180°.

Figure 6. - Concluded. Experimental and theoretical axial variation of pressure-coefficient increment due to angle of attack.

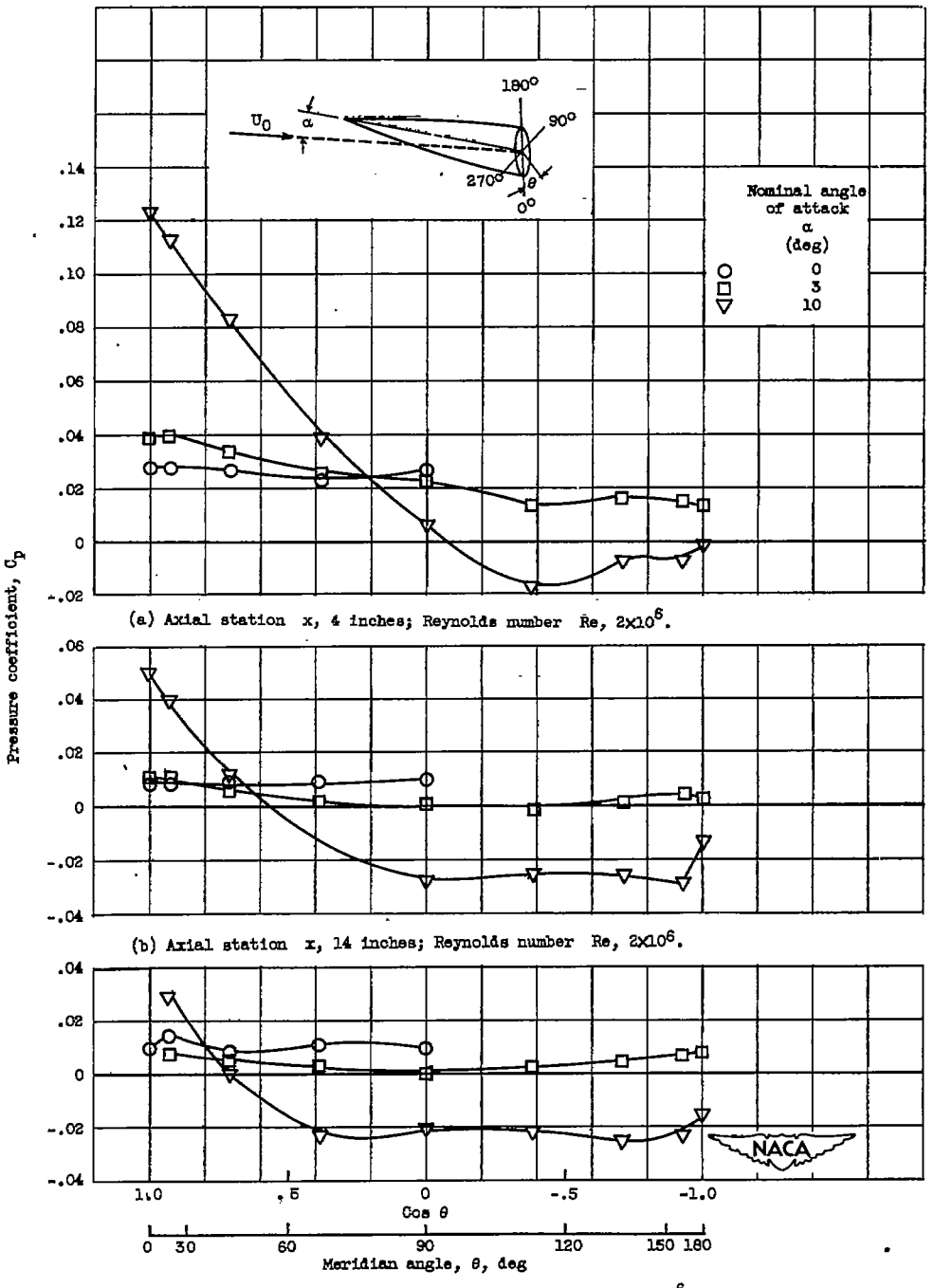

(a) Axial station x, 4 inches; Reynolds number Re, 2×10^6.

(b) Axial station x, 14 inches; Reynolds number Re, 2×10^6.

(c) Axial station x, 20.5 inches; Reynolds number Re, 2×10^6.

Figure 7. - Experimental variation of pressure coefficient with meridian angle for given axial station.

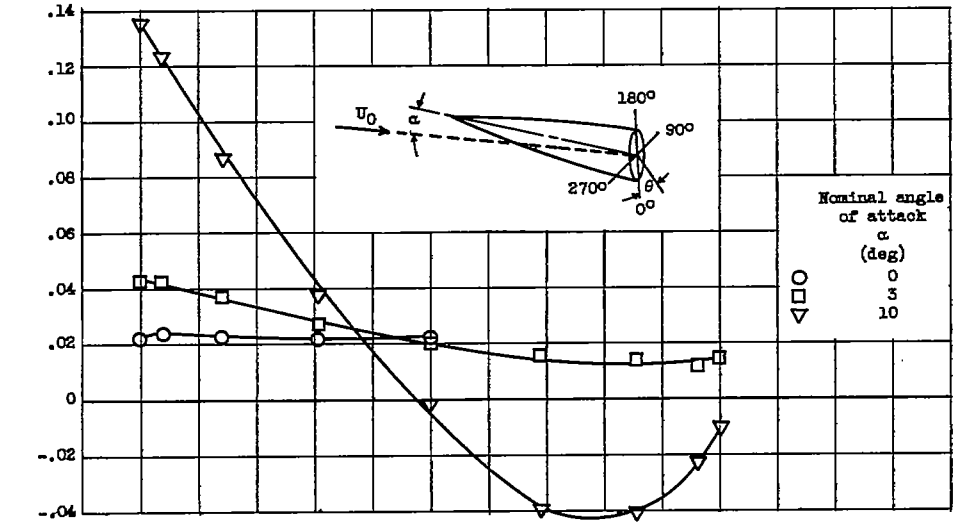

(d) Axial station x, 4 inches; Reynolds number Re, 8×10^6.

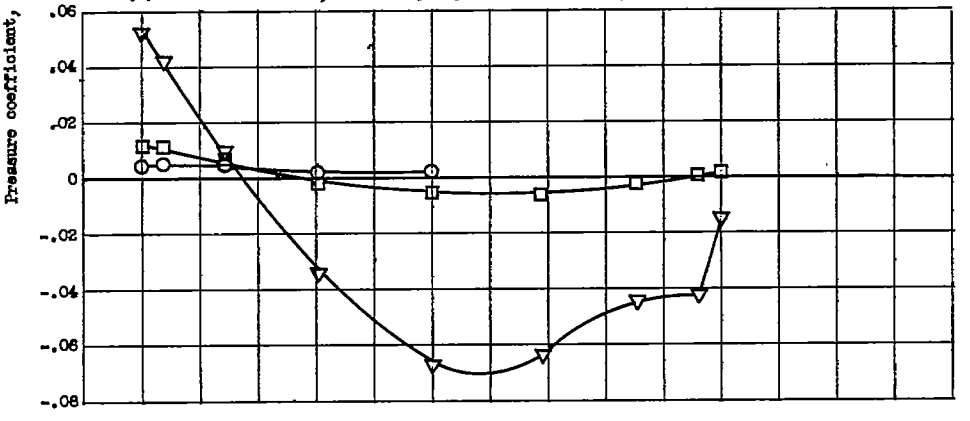

(e) Axial station x, 14 inches; Reynolds number Re, 8×10^6.

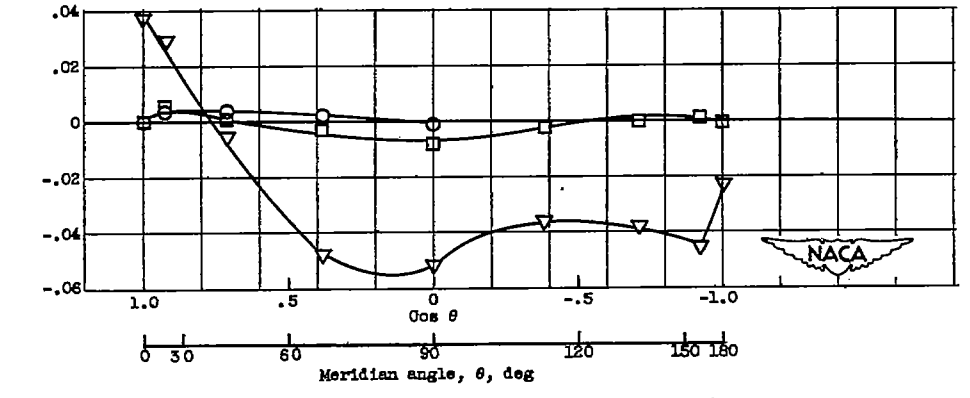

(f) Axial station x, 20.5 inches; Reynolds number Re, 8×10^6.

Figure 7. - Continued. Experimental variation of pressure coefficient with meridian angle for given axial station.

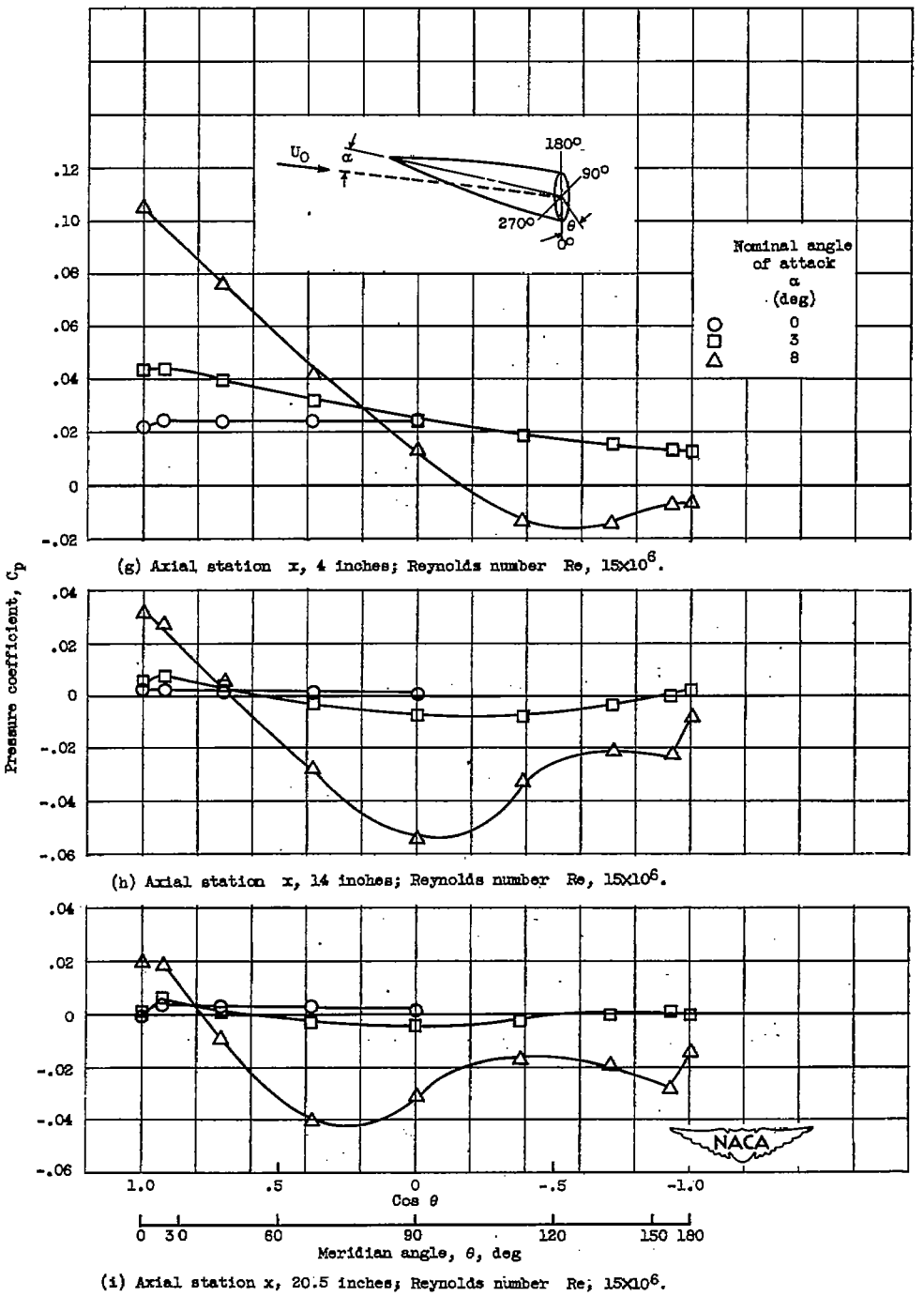

(g) Axial station x, 4 inches; Reynolds number Re, 15×10^6.

(h) Axial station x, 14 inches; Reynolds number Re, 15×10^6.

(i) Axial station x, 20.5 inches; Reynolds number Re; 15×10^6.

Figure 7. - Concluded. Experimental variation of pressure coefficient with meridian angle for given axial station.

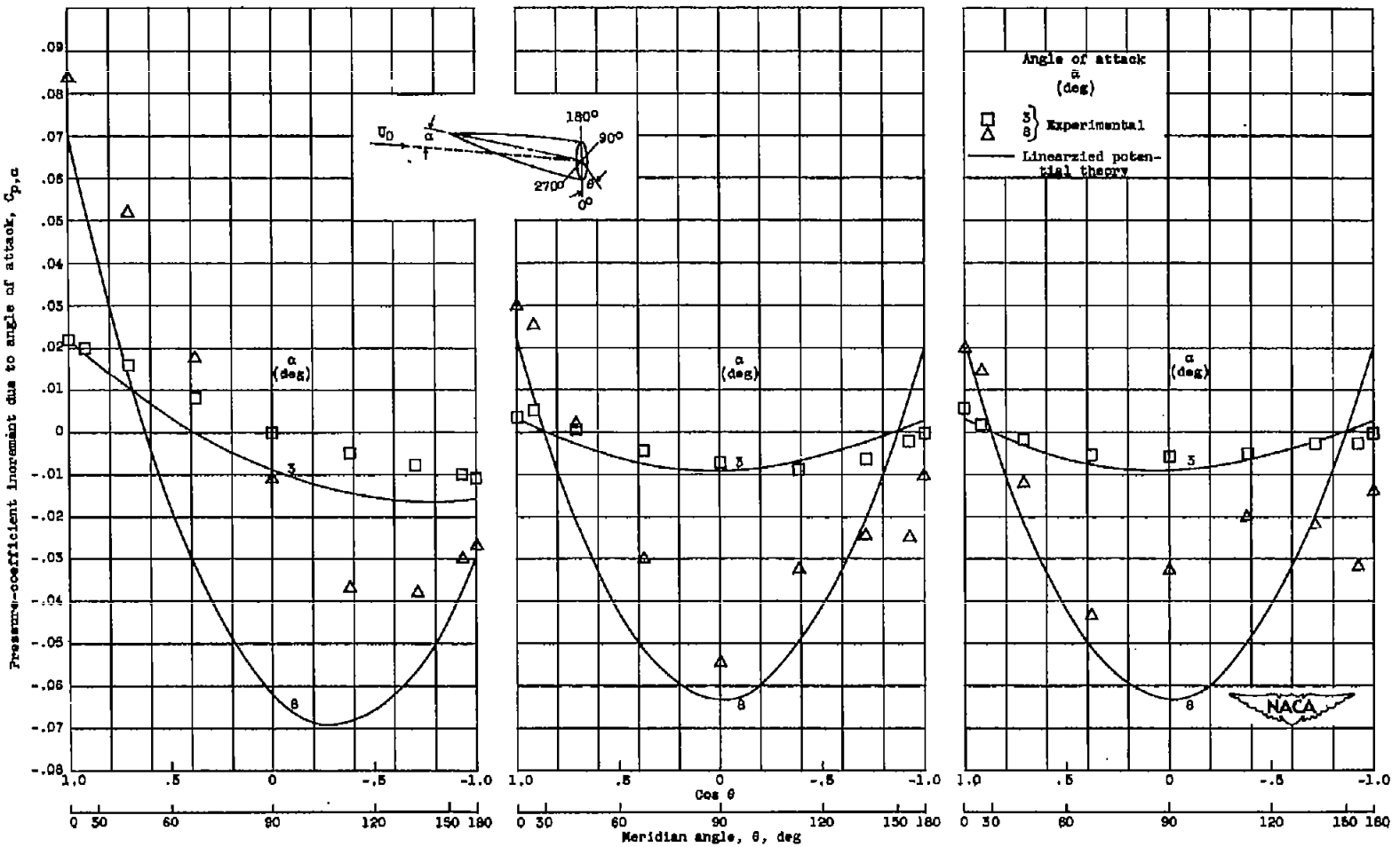

(a) Axial station x, 4 inches; Reynolds number Re, 15×10^6.

(b) Axial station x, 14 inches; Reynolds number Re, 15×10^6.

(c) Axial station x, 20.5 inches; Reynolds number Re, 15×10^6.

Figure 8. - Theoretical and experimental variation of pressure-coefficient increment due to angle of attack with angular position for two angles of attack.

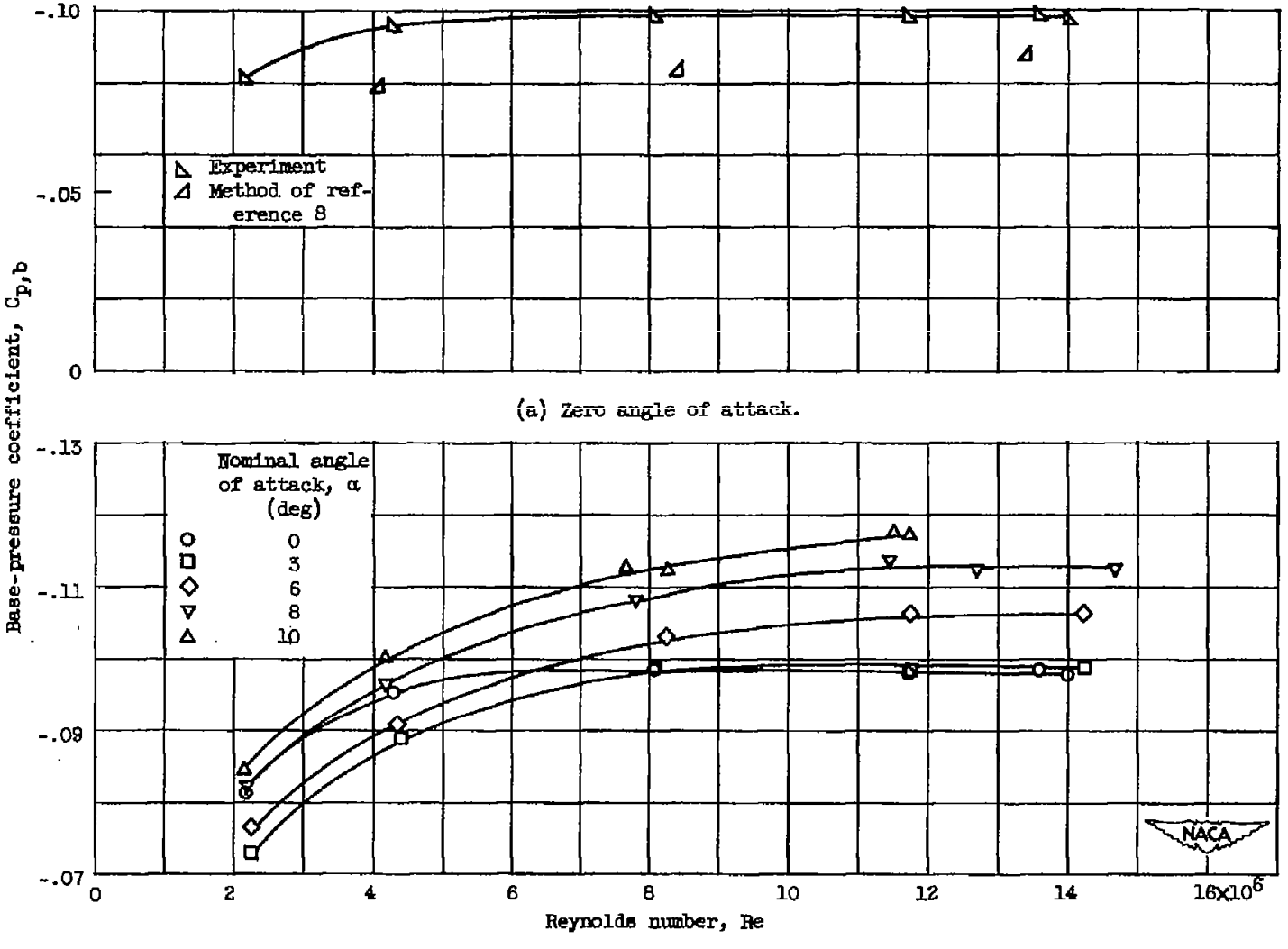

(a) Zero angle of attack.

(b) Five angles of attack.

Figure 9. - Variation of base-pressure coefficient with Reynolds number.

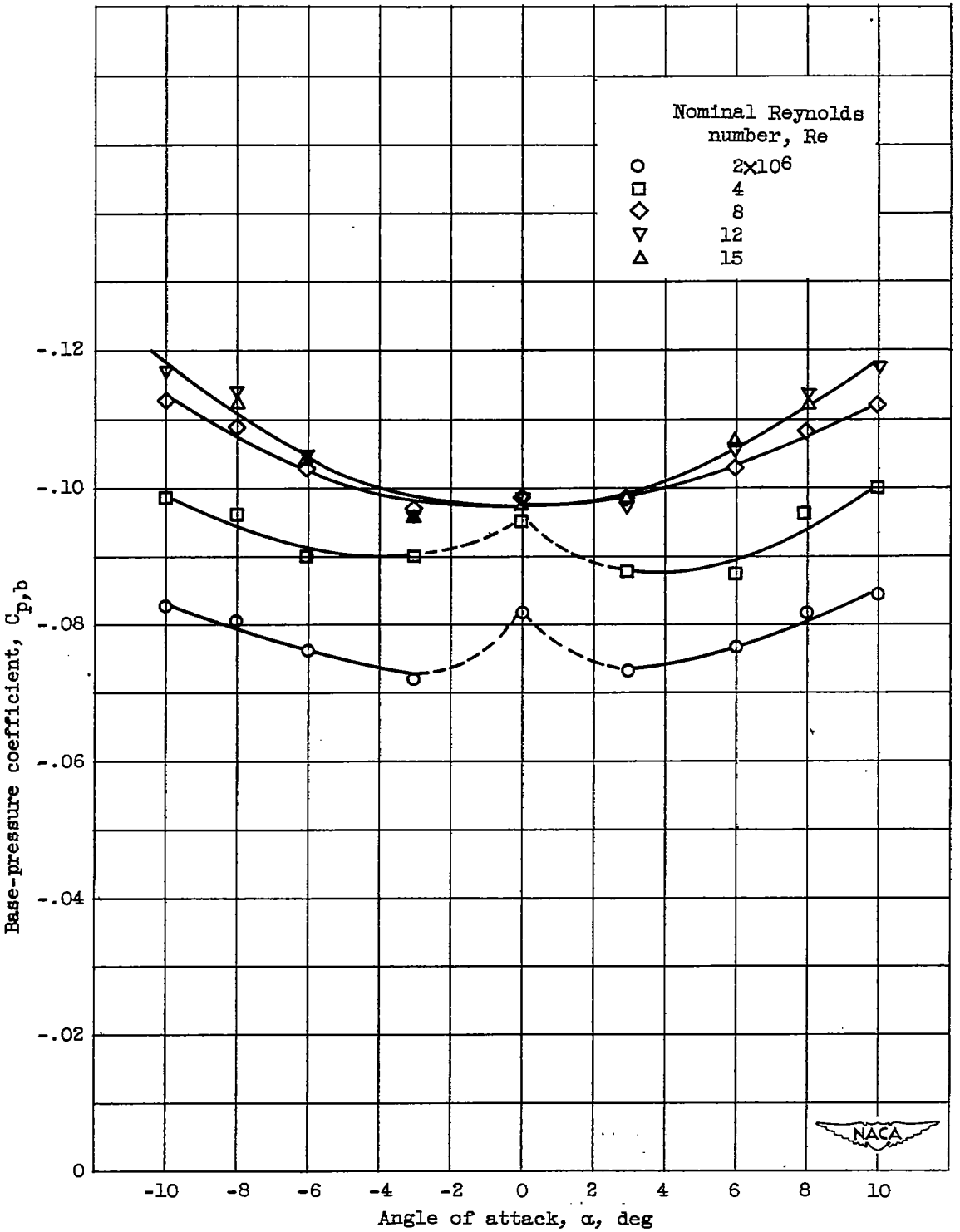

Figure 10. - Variation of base-pressure coefficient with angle of attack for Reynolds numbers of 2×10^6, 4×10^6, 8×10^6, 12×10^6, and 15×10^6.

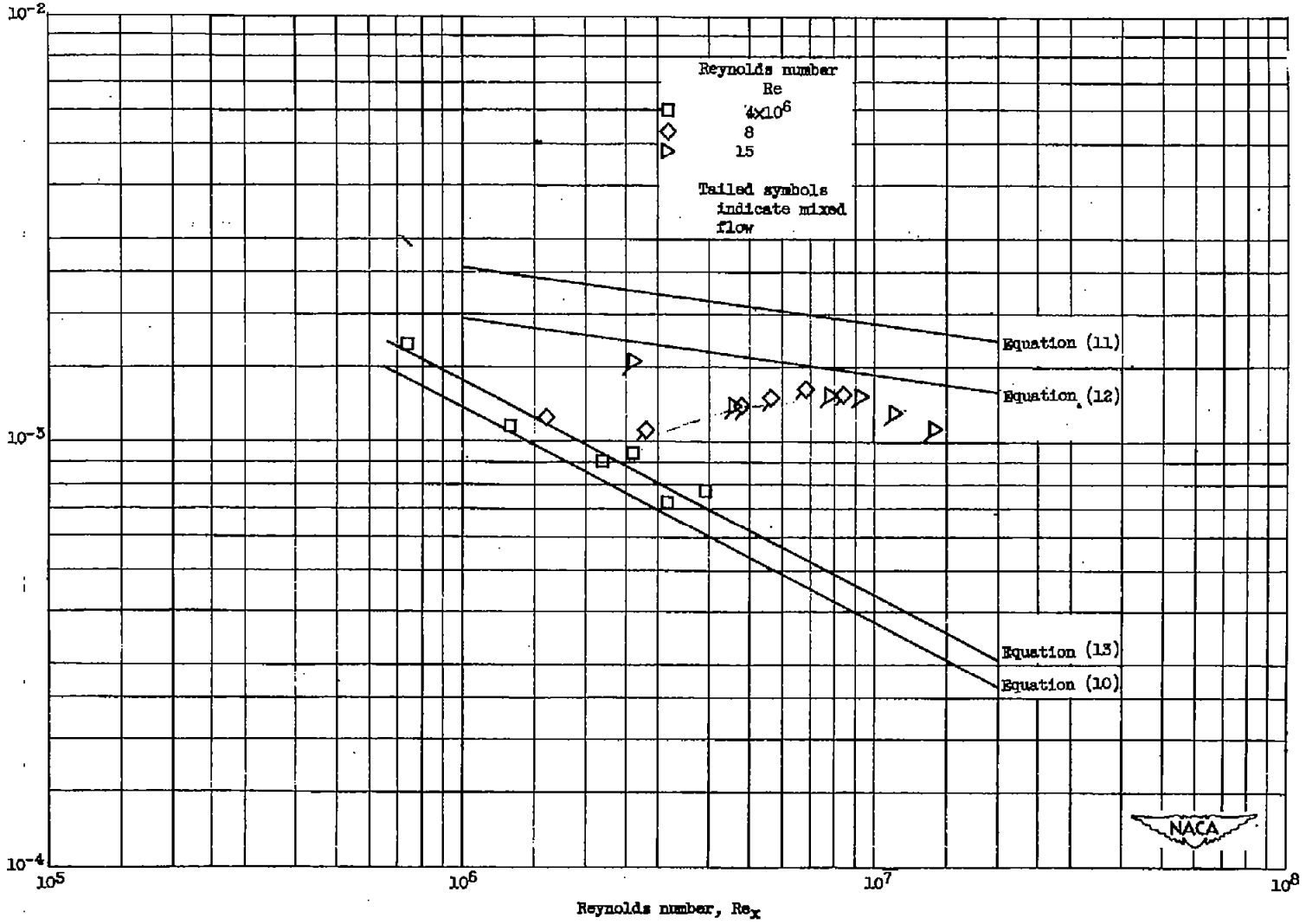

Figure 11. - Variation of mean friction-drag coefficient with Reynolds number for zero angle of attack.

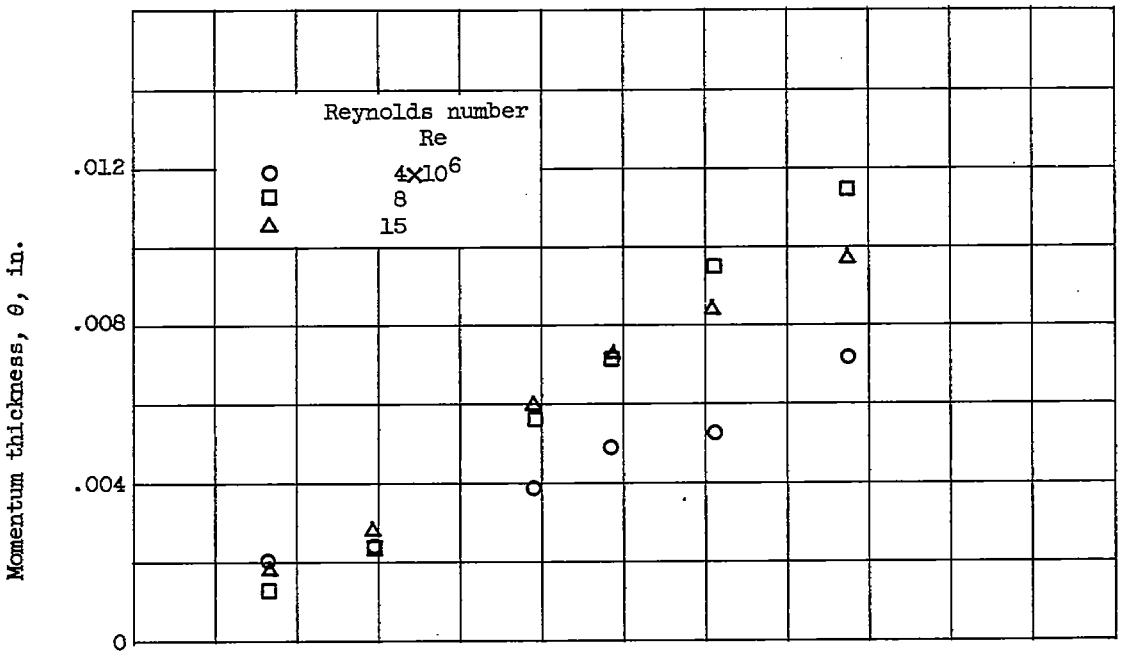

(a) Variation of momentum thickness with axial station.

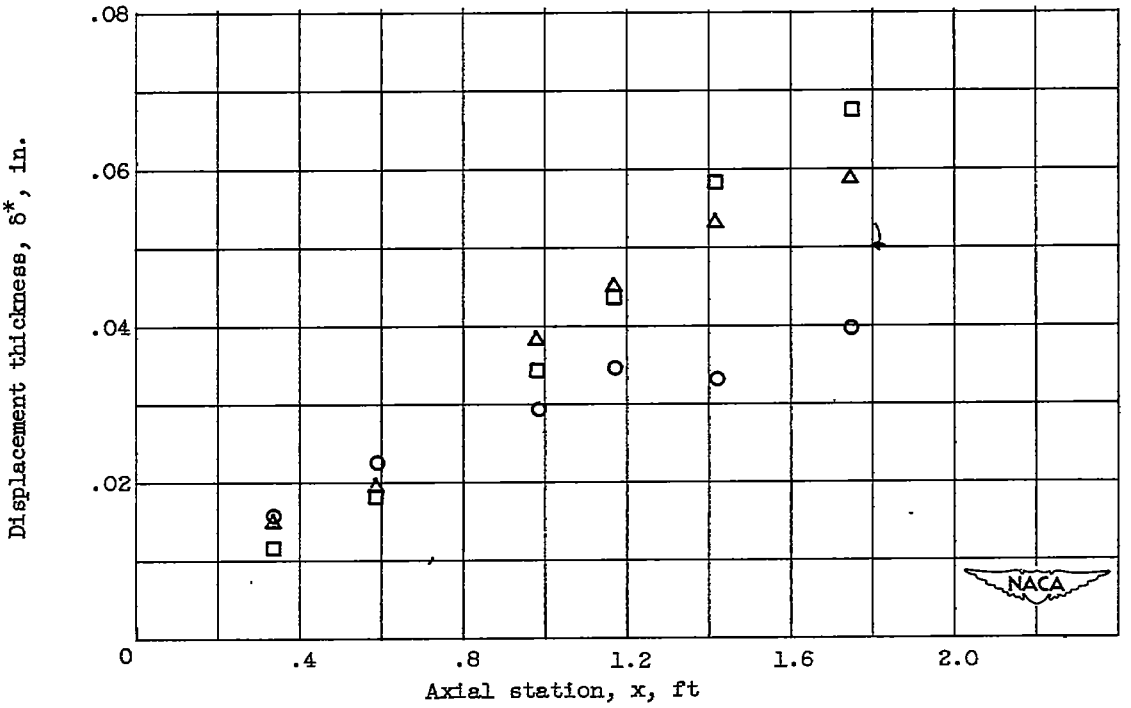

(b) Variation of displacement thickness with axial station.

Figure 12. - Variation of momentum and displacement thicknesses with axial station at Mach number of 3.12 for Reynolds numbers of 4×10^6, 8×10^6, and 15×10^6.

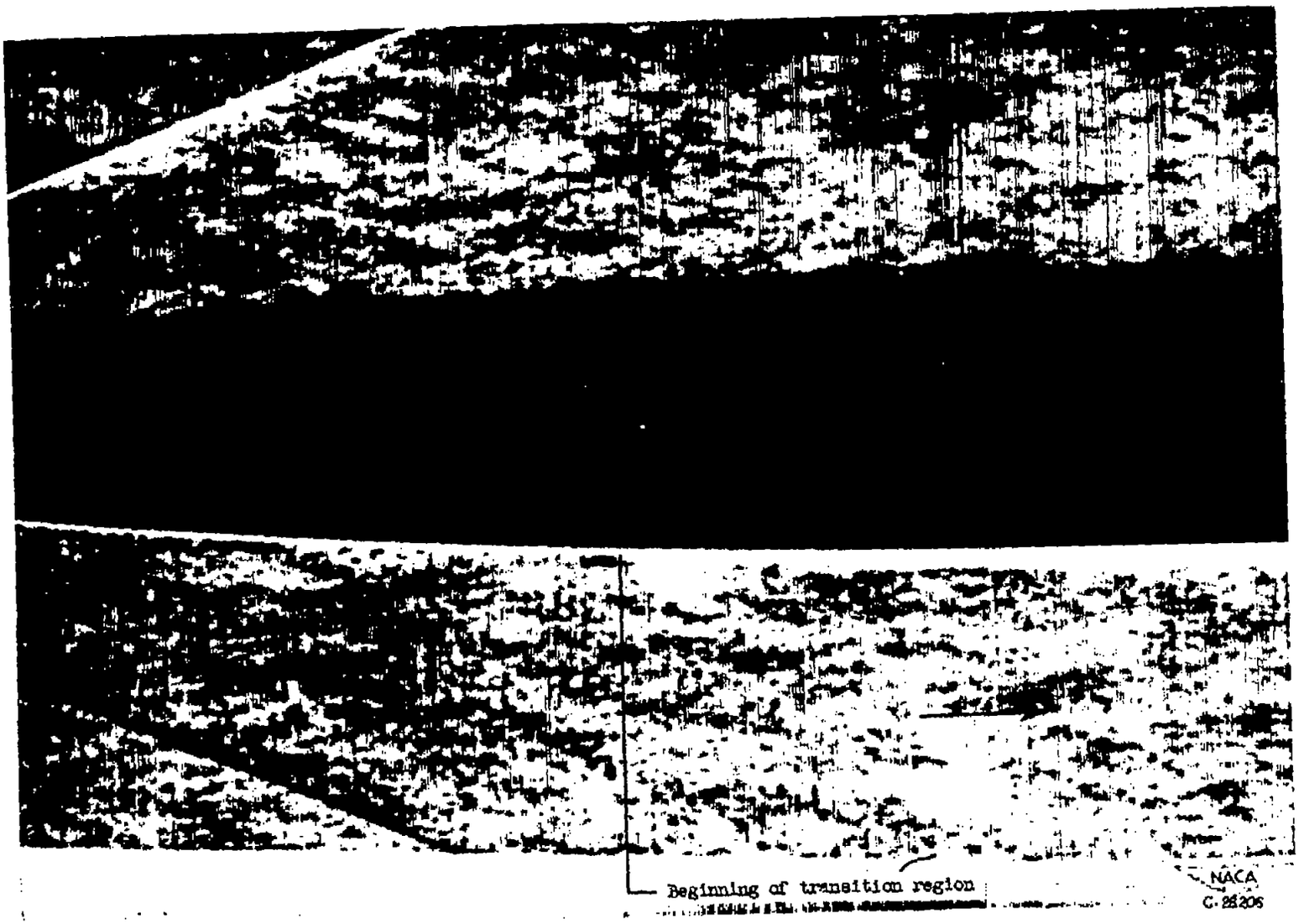

Figure 13. - Schlieren of boundary-layer transition at a Reynolds number of 8×10^6.

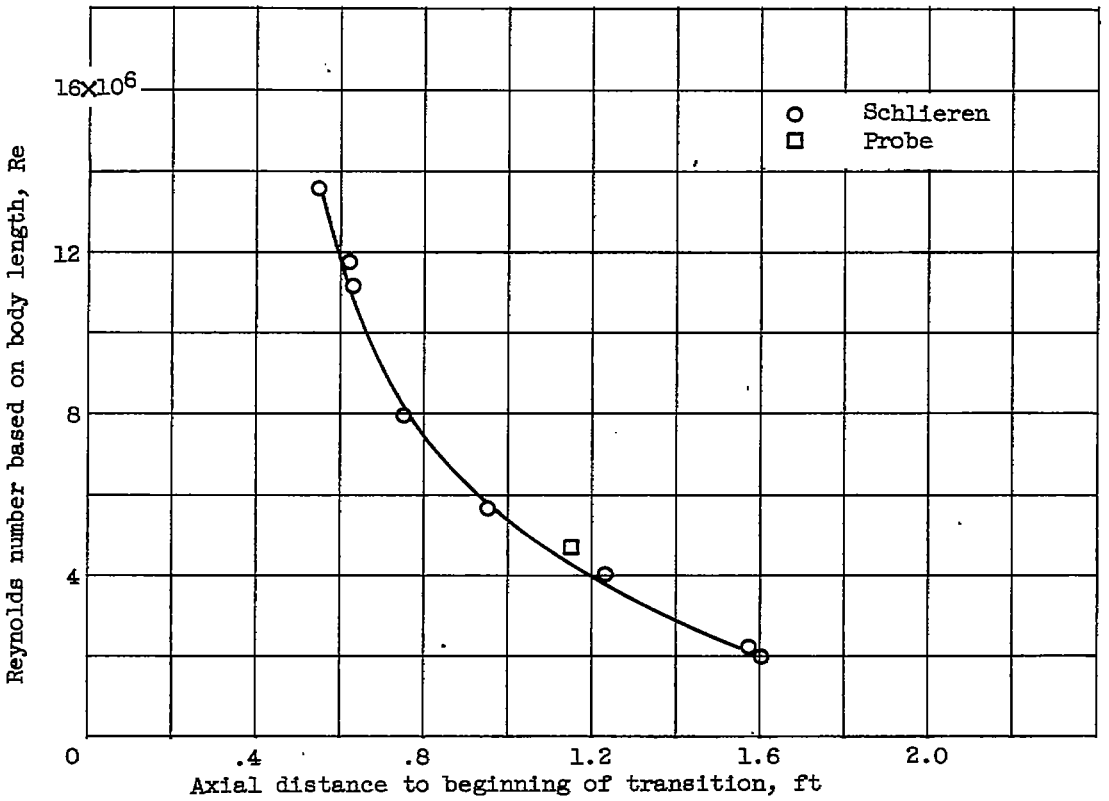

(a) Effect of free-stream Reynolds number upon axial distance to beginning of transition.

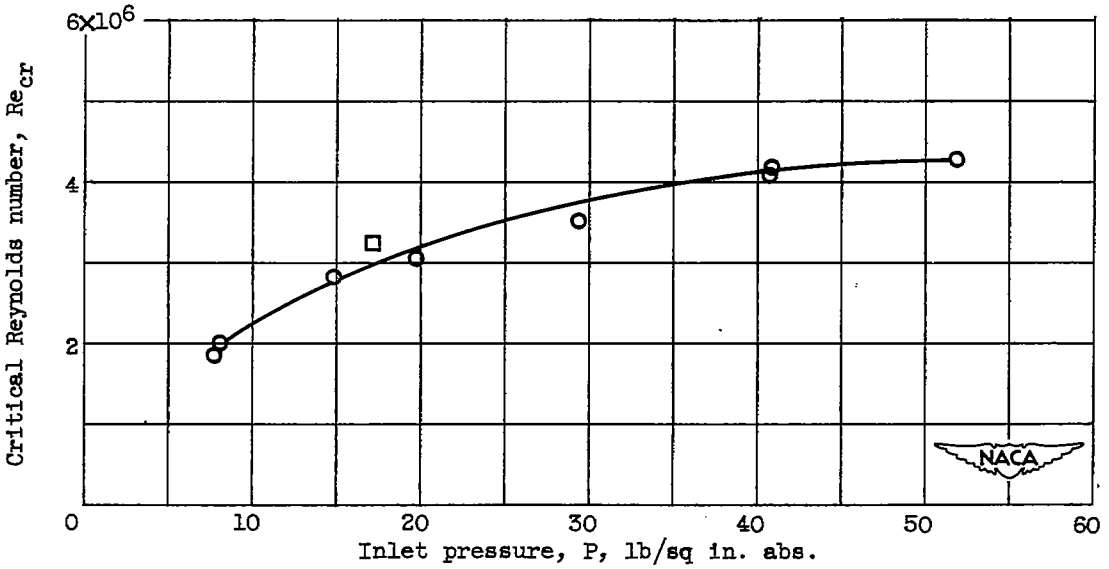

(b) Effect of inlet pressure upon critical Reynolds number.

Figure 14. - Boundary-layer transition at Mach number of 3.12.

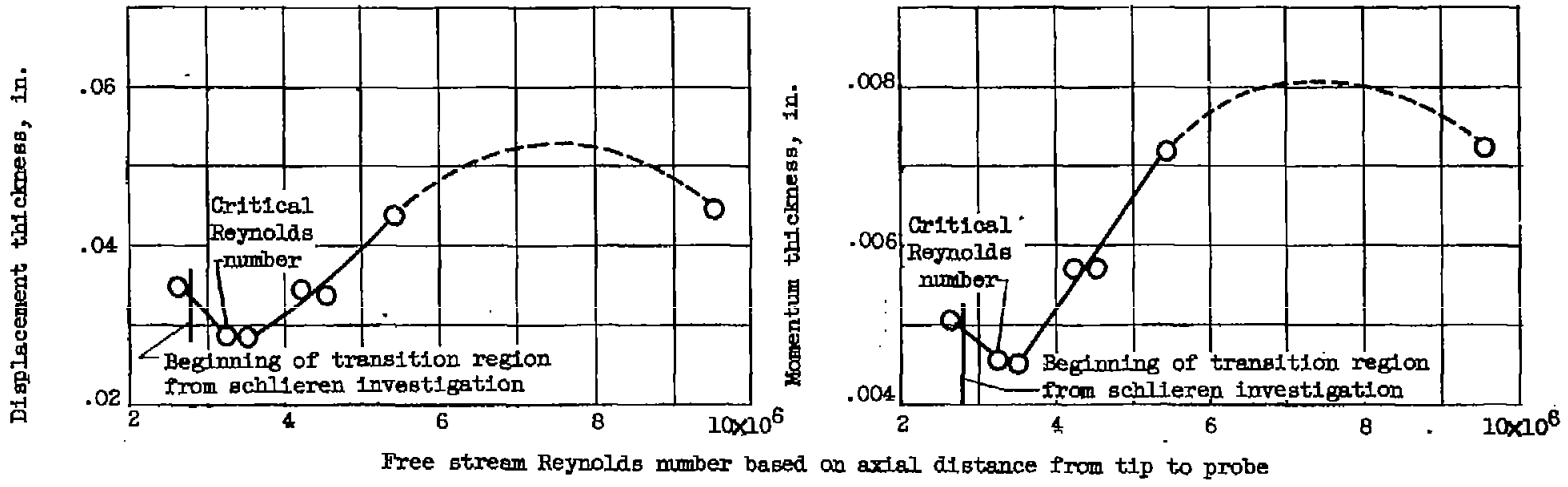

Figure 15. - Variation of boundary-layer momentum and displacement thicknesses with free-stream Reynolds number (axial distance to probe). Probe station, 1.17 feet from tip; Mach number, 3.12.

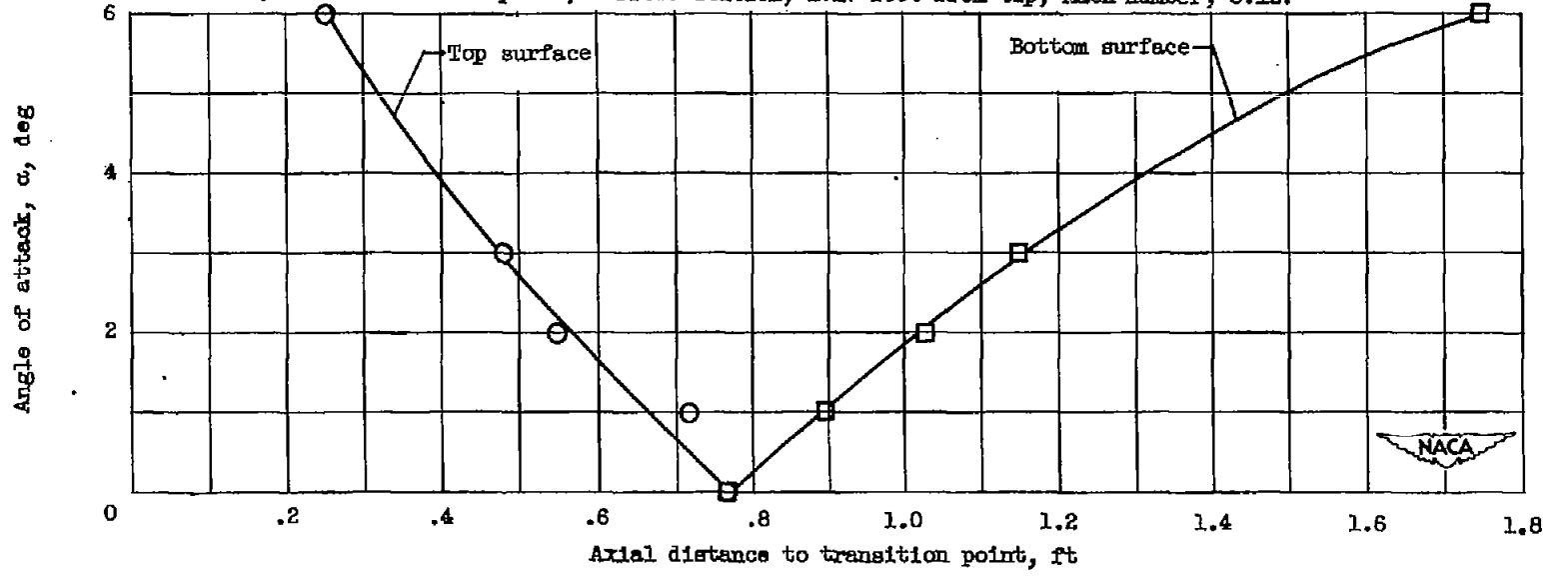

Figure 16. - Variation of boundary-layer transition with angle of attack. Mach number 3.12; Reynolds number, 8×10^6.

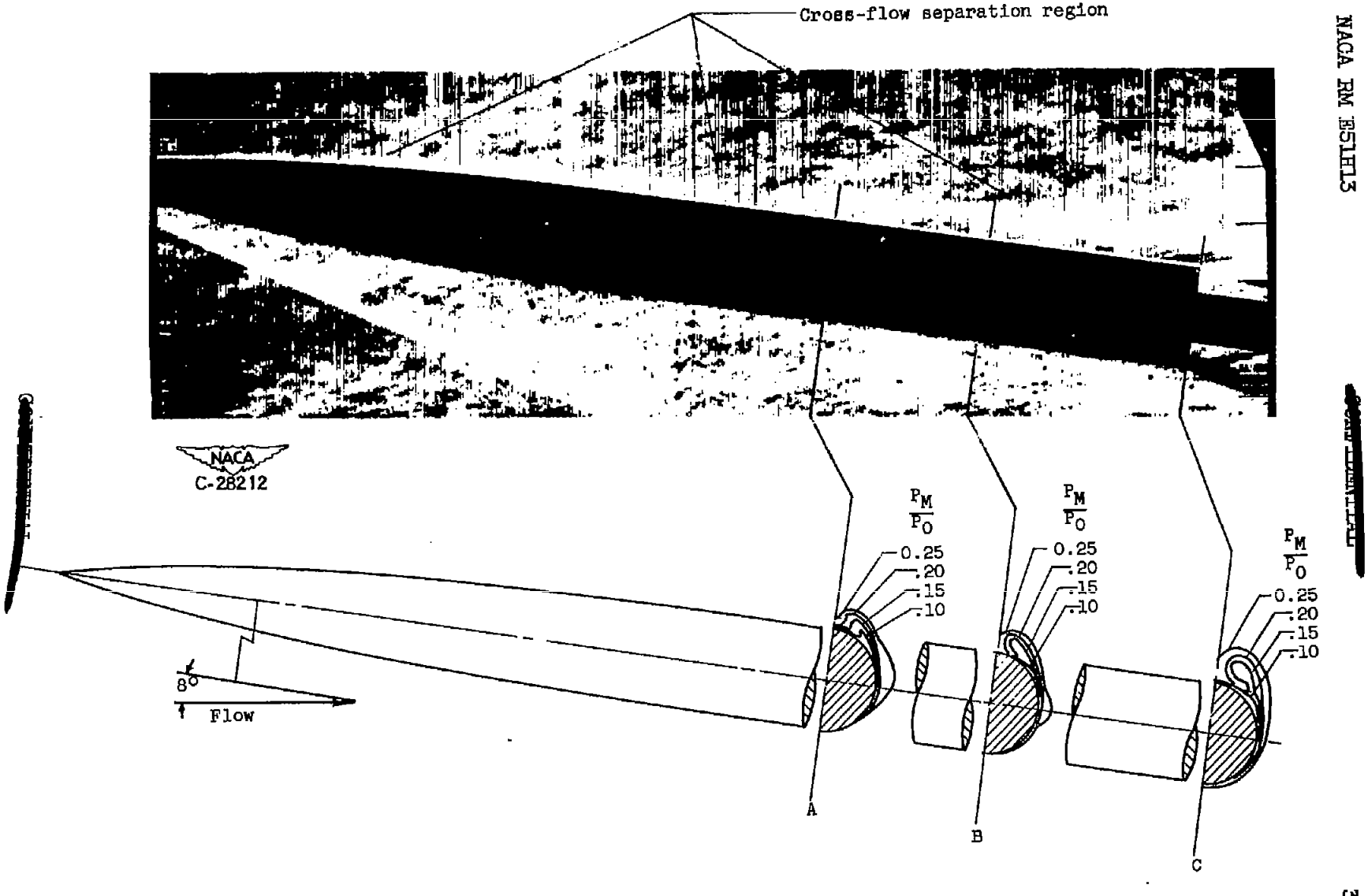

Figure 17. - Pitot survey and schlieren of cross-flow separation at Reynolds number of 8×10^6, Mach number of 3.12, and free-stream pressure ratio P_M/P_O of 0.296.

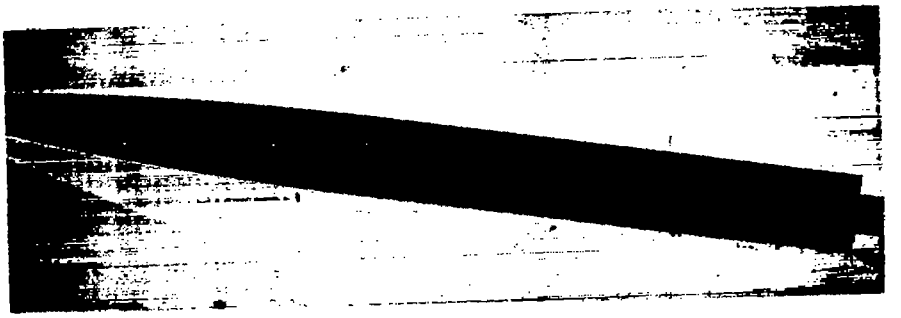

(a) Reynolds number, 4×10^6.

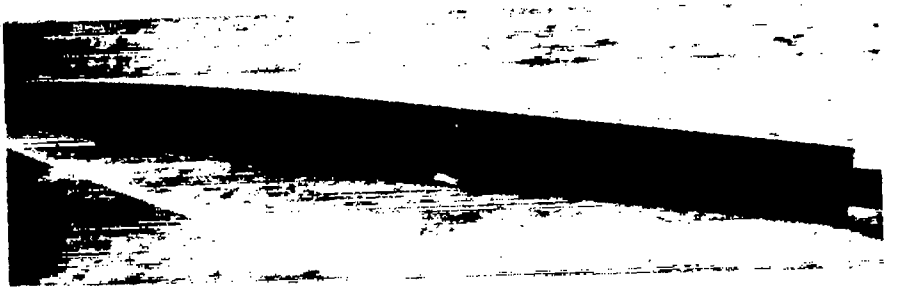

(b) Reynolds number, 8×10^6.

(c) Reynolds number, 12×10^6.

(d) Reynolds number, 15×10^6.

NACA C-28207

Figure 18. - Variation of cross-flow separation with Reynolds number at angle of attack of 8°.

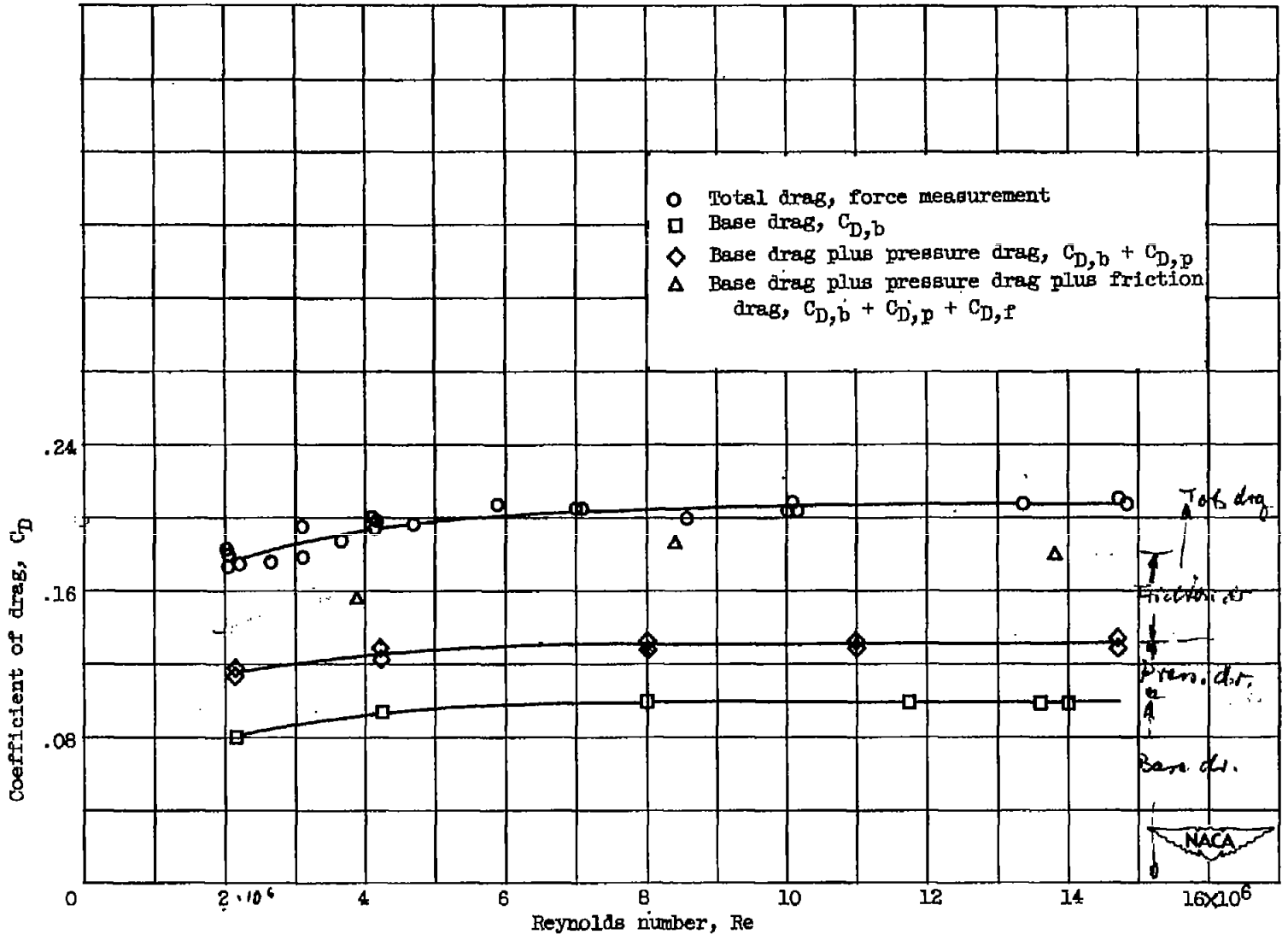

Figure 19. - Variation of drag coefficient with Reynolds number for zero angle of attack.

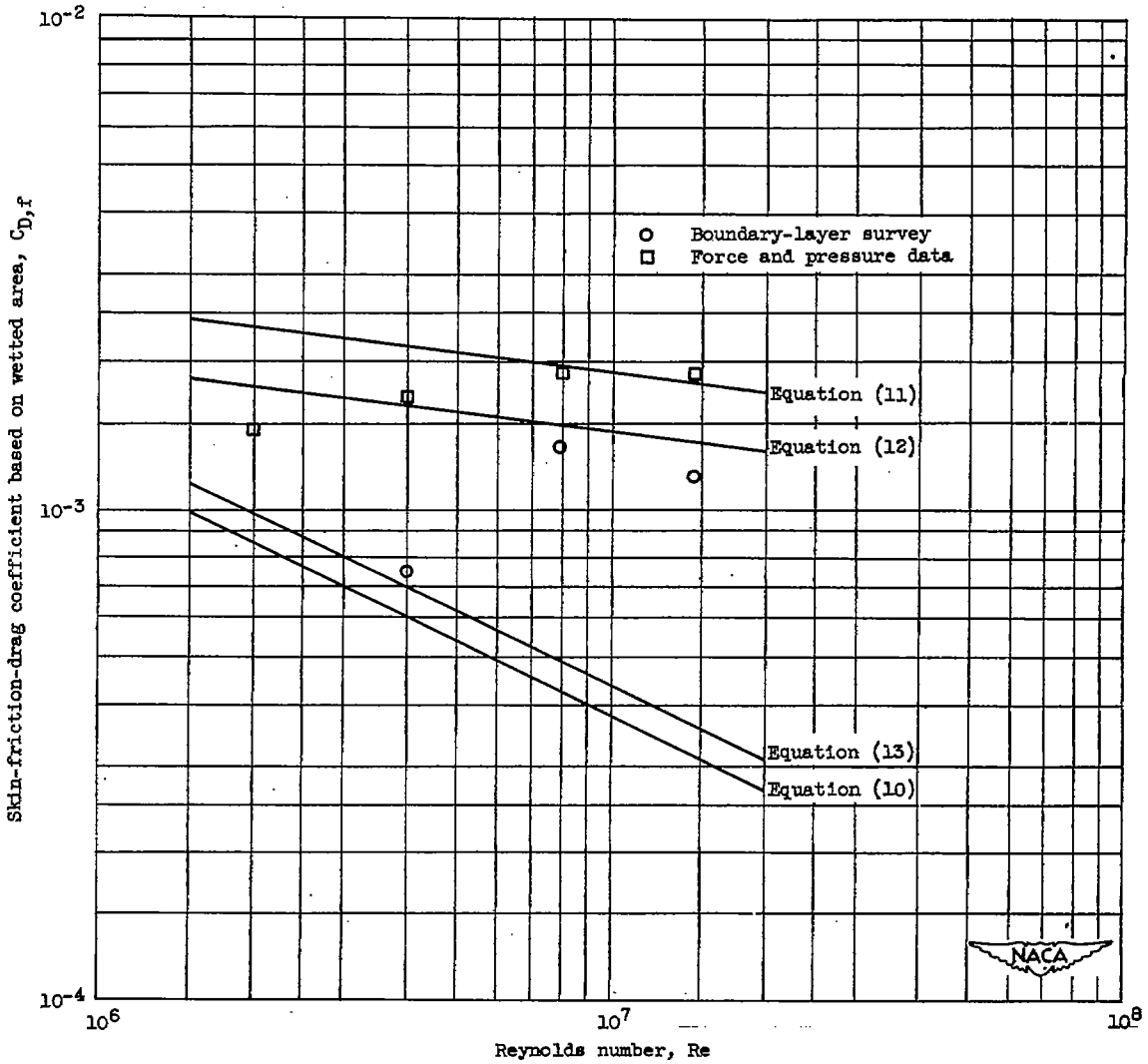

Figure 20. - Variation of skin-friction-drag coefficient with Reynolds number for zero angle of attack.

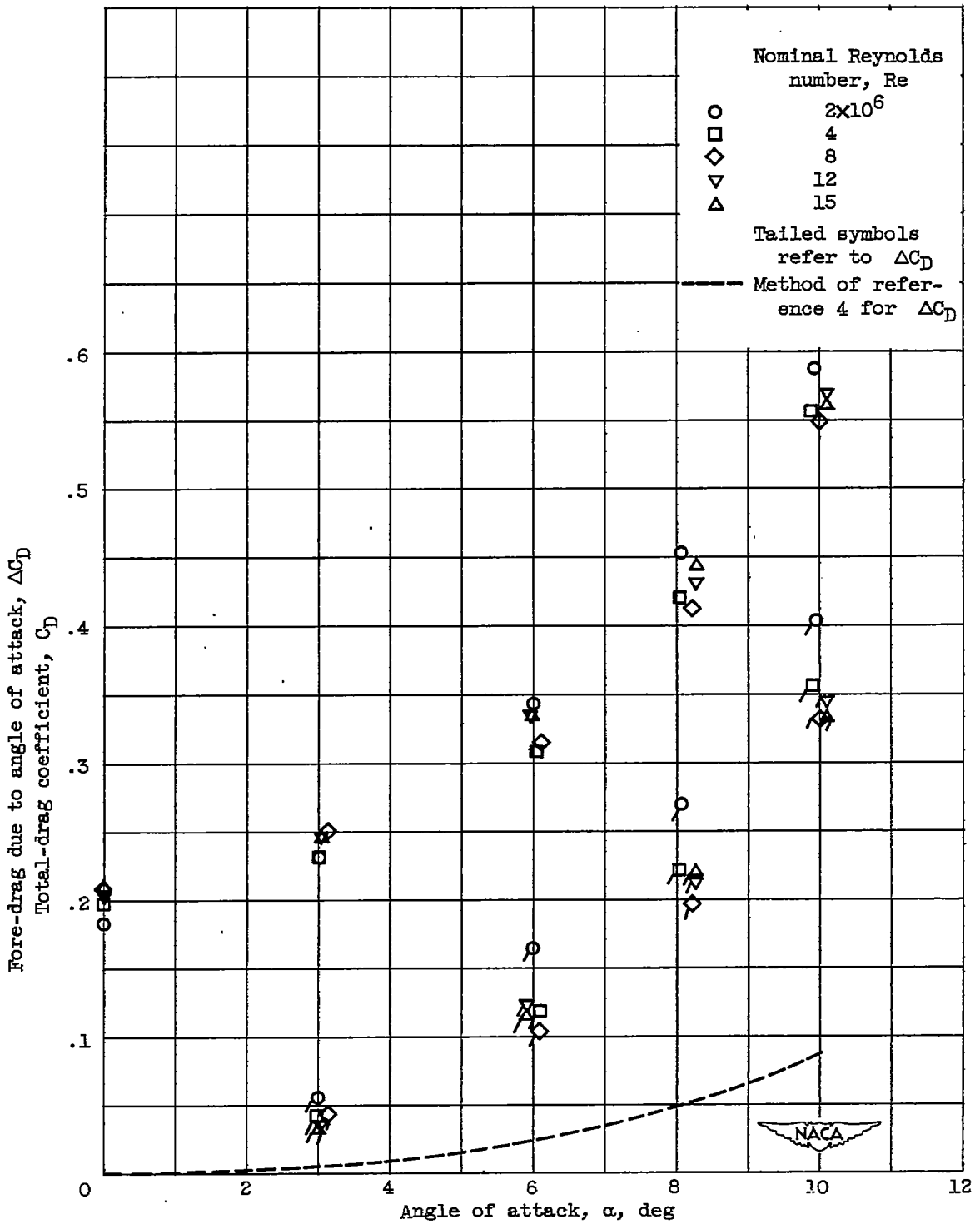

Figure 21. - Variation of drag coefficient with angle of attack for five Reynolds numbers.

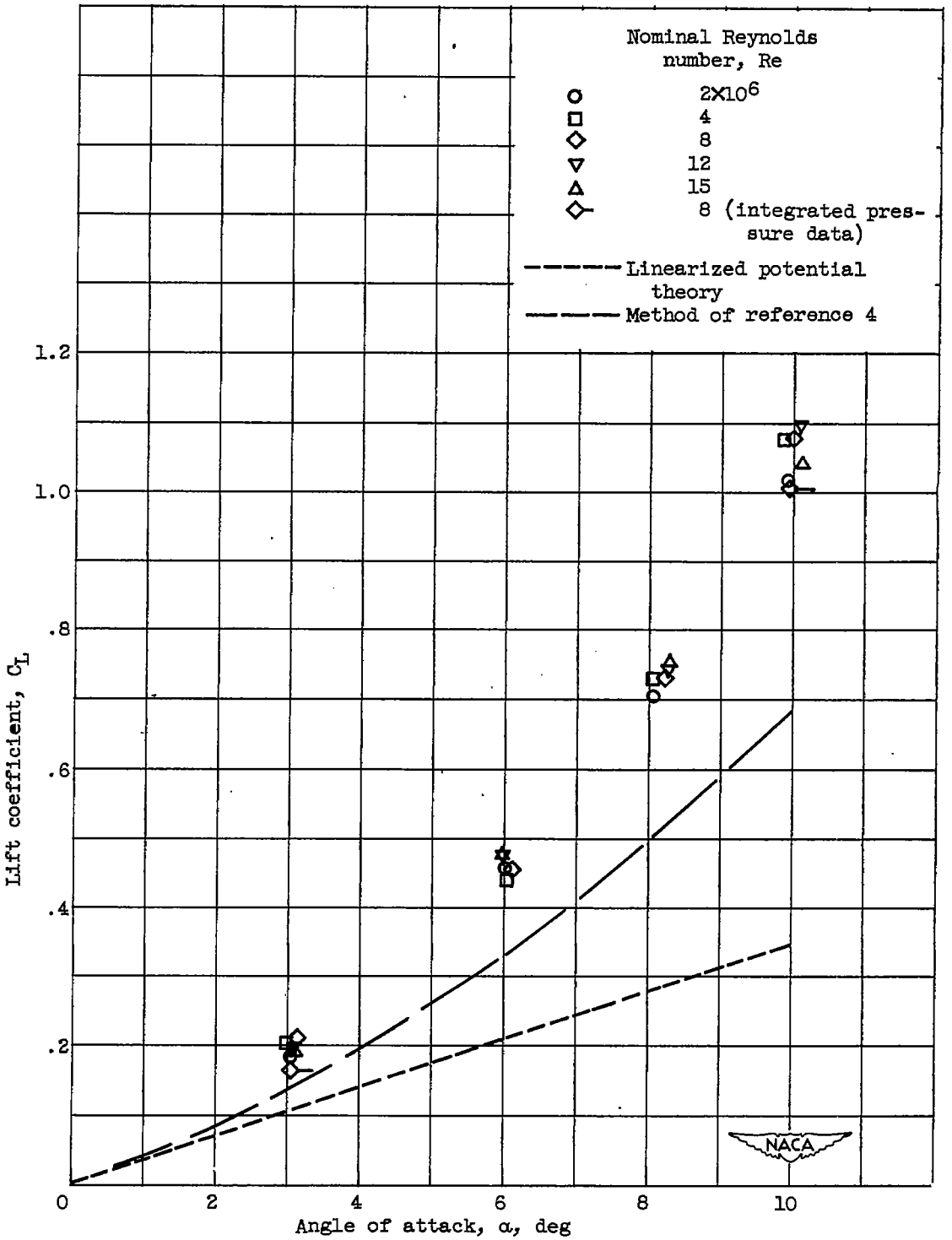

Figure 22. - Variation of lift coefficient with angle of attack for five Reynolds numbers.

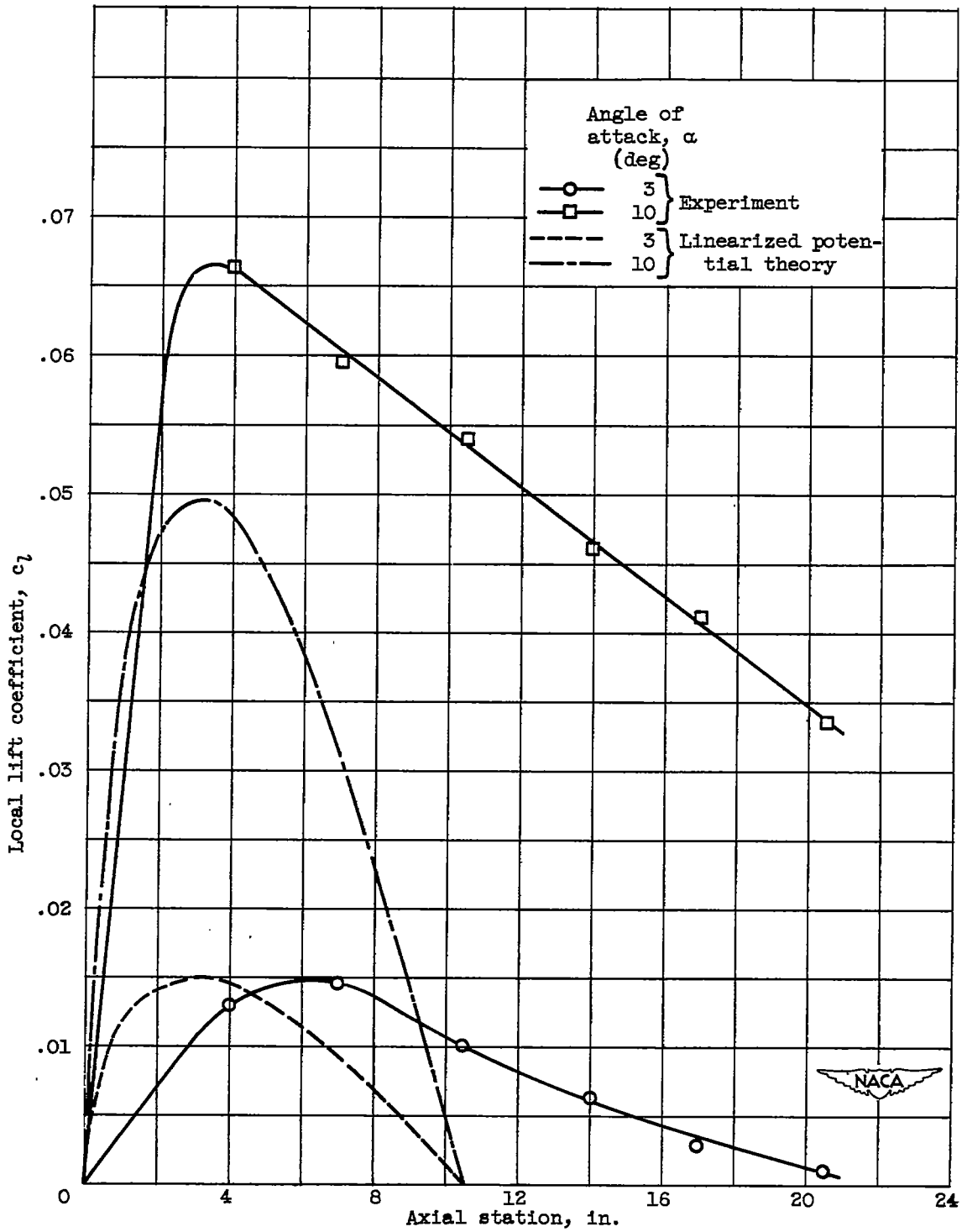

Figure 23. - Variation of local lift coefficient with axial station for two angles of attack. Nominal Reynolds number, 8×10^6.

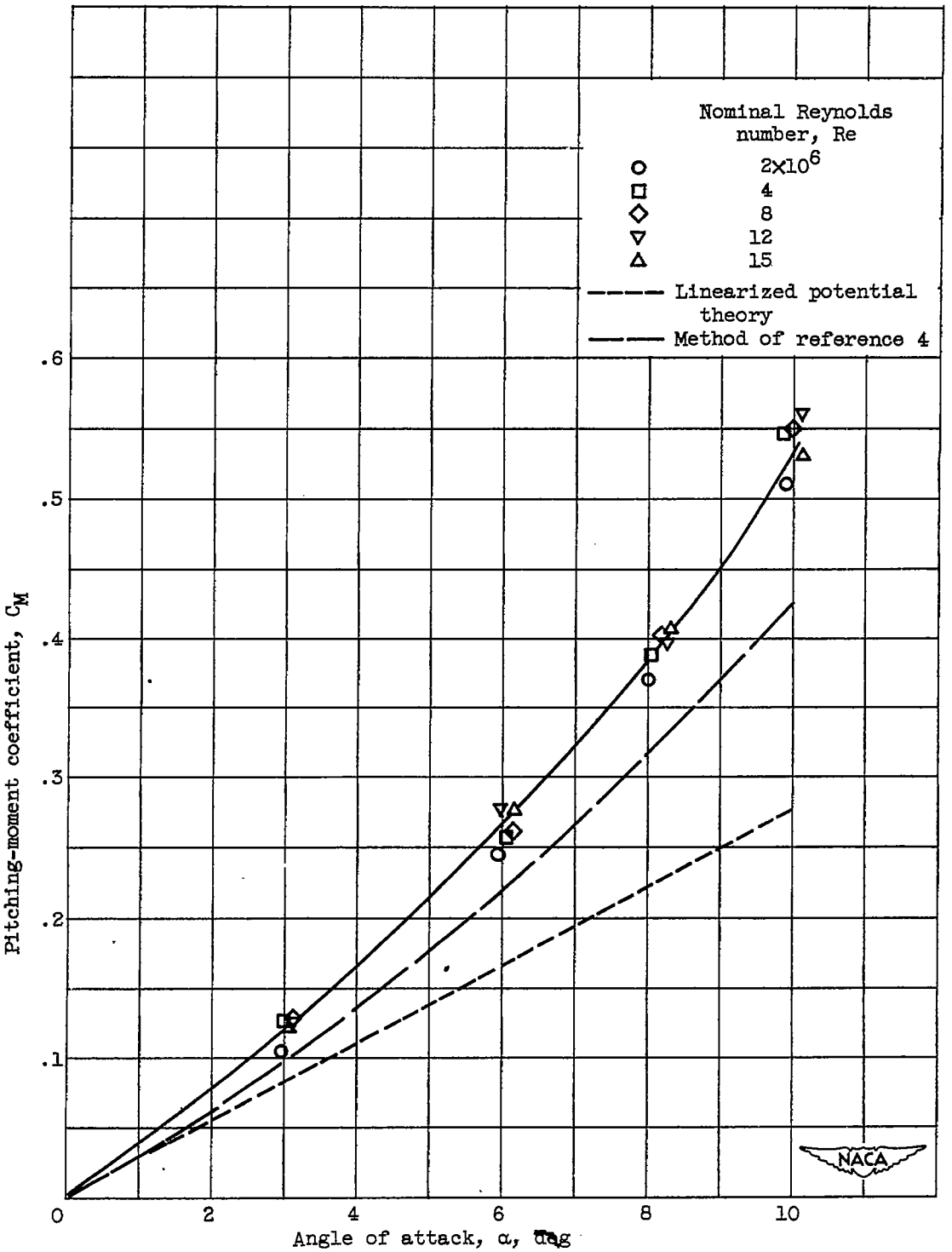

Figure 24. - Variation of pitching-moment coefficient with angle of attack for five Reynolds numbers.

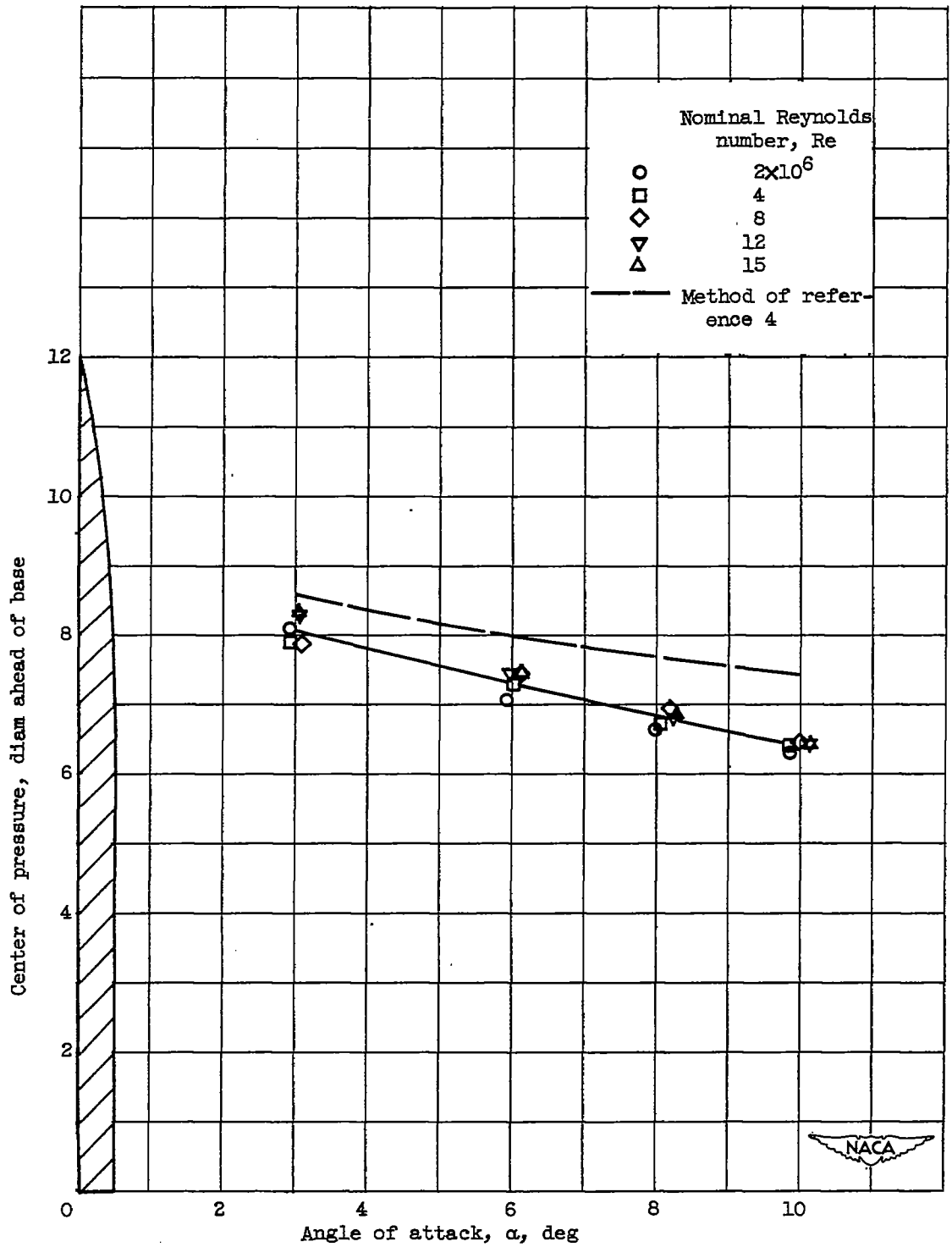

Figure 25. - Variation of center of pressure with angle of attack for five Reynolds numbers.

NACA-Langley - 11-13-51 - 400